

1  
2  
3  
4  
5  
6  
7 Diabatic Eddy Forcing Increases Persistence and Opposes Propagation of the Southern Annular  
8 Mode in MERRA2

Samuel Smith<sup>1\*</sup>, Jian Lu<sup>2</sup>, Paul W. Staten<sup>1</sup>

<sup>1</sup>Indiana University, Bloomington, IN <sup>2</sup>Pacific Northwest National Laboratory, Richland, WA

9 \*Contact information: 1001 E. 10<sup>th</sup> St., Bloomington, IN 47408; [samjsmit@iu.edu](mailto:samjsmit@iu.edu)

10    **Abstract**

11    As a dominant mode of jet variability on sub-seasonal timescales, the Southern Annular Mode  
12    (SAM) provides a window into how the atmosphere can produce internal oscillations on longer-  
13    than-synoptic timescales. While SAM's existence can be explained by dry, purely barotropic  
14    theories, the timescale for its persistence and propagation is set by a lagged interaction  
15    between barotropic and baroclinic mechanisms, making the exact physical mechanisms  
16    challenging to identify and to simulate, even in latest generation models. By analyzing the eddy  
17    momentum flux convergence budget in the MERRA2 reanalysis, we contend that diabatic  
18    processes, such as condensation and radiative heating, are the main contributors to SAM's  
19    persistence in its stationary regime, as well as the key for preventing propagation in this  
20    regime. In SAM's propagating regime, baroclinic and diabatic feedbacks also dominate the  
21    eddy-jet feedback. However, propagation is initiated by barotropic shifts in upper-level wave-  
22    breaking and then sustained by a baroclinic response, leading to a roughly 60-day oscillation  
23    period. This barotropic propagation mechanism has been identified in dry, idealized models,  
24    but here we show evidence of this mechanism for the first time in reanalysis. The diabatic  
25    feedbacks on SAM are consistent with modulation of the storm track latitude by SAM, altering  
26    the emission temperature and cloud cover over individual waves. Therefore, we suggest that  
27    any attempts to improve SAM representation in models must consider the influence of storm  
28    track location, as well as cloud and moisture parameterizations.

29

30    **Significance Statement**

31    As they circumnavigate the planet, the tropospheric jet streams slowly drift north and south  
32    over about 30 days, longer than the normal limit of weather prediction. Understanding the  
33    source of this “memory” could improve our knowledge of how the atmosphere organizes itself  
34    and our ability to make long-term forecasts. Current theories have identified several possible  
35    internal atmospheric interactions responsible for this memory. Yet most of the theories for  
36    understanding the jets’ behavior assume that the behavior is only weakly influenced by  
37    atmospheric water vapor. We show that this assumption cannot be used to understand jet  
38    persistence. Instead, clouds and precipitation are more important contributors than internal  
39    “dry” mechanisms to this memory in fluctuations of the Southern Hemisphere jet.

40

41     **1. Introduction**

42                 The most ubiquitous modes of variability in extratropical zonal winds are the barotropic  
43     “annular” modes, subseasonal to interannual fluctuations in tropospheric jet latitude which  
44     evoke a contracting and dilating annulus (Rossby and Willet 1948; Kidson 1988a; Thompson and  
45     Wallace 2000; Thompson et al. 2000). These annular dynamics are generated by a coherent  
46     shift of upper-tropospheric wave breaking and an associated shift of the eddy momentum flux  
47     convergence (EMFC) which drives the barotropic jets (Thompson and Wallace 2000; Lorenz and  
48     Hartmann 2001). Even highly idealized atmospheric models can reproduce the essential  
49     ingredients of annular modes (Lee and Feldstein 1996; Barnes et al. 2010; Lutsko and Hell  
50     2021), evidence that they are both fundamental and theoretically established.

51                 Given their low-frequency variability, barotropic annular modes (hereafter, annular  
52     modes) have been identified as a potential source of predictability in the atmosphere at longer-  
53     than-synoptic timescales (Kidson 1988b; Baldwin and Dunkerton 2001; Son and Lee 2006). Such  
54     efforts, however, have been complicated by difficulties in accurately simulating the annular  
55     mode timescale (Gerber et al. 2008), which is over-predicted even in latest generation models  
56     (Bracegirdle et al. 2020). And these model timescale biases have implications beyond  
57     predictability. Although there is much debate, these biases may imply an overestimation of the  
58     jet response to external forcing (Gritsun and Branstator 2007; Ring and Plumb 2008; Kidston  
59     and Gerber 2010; but also, Simpson and Polvani 2016; Hassanzadeh and Kuang 2016).

60                 Perhaps the foremost mechanism to explain annular mode persistence is a positive  
61     eddy-jet feedback (Lorenz and Hartmann 2001; Simpson et al. 2013; Nie et al. 2014; Ma et al.  
62     2017; Lubis and Hassanzadeh 2020). The clearest evidence for the feedback is a positive

63 correlation between the anomalous jet latitude and the annular-mode-induced EMFC seven to  
64 ten days later (Lorenz and Hartmann 2001). However, the feedback does not appear in all  
65 seasons, and it is plausible that the proximate eddy-jet feedback is a manifestation of low-  
66 frequency variability, perhaps by way of the stratosphere (Byrne et al. 2016; Saggioro and  
67 Shepherd 2019). Nonetheless, eddy-jet feedbacks have been unambiguously demonstrated in  
68 idealized models forced with annular mode anomalies (Ma et al. 2017).

69 Another potential mechanism explains the increased persistence of annular modes  
70 through an interaction between the jet-shifting and jet-pulsing modes of variability (Lubis and  
71 Hassanzadeh 2020), typically defined as the first and second empirical orthogonal functions  
72 (EOFs) of zonal-mean zonal wind. While the two EOFs are uncorrelated at short lags (by  
73 construction), at longer lags, an equatorward shift of the jet is often preceded by a weakened  
74 jet and followed by a stronger jet. This interaction produces a slow meridional propagation of  
75 zonal wind anomalies (Lee et al. 2007; Sheshadri and Plumb 2017), and it explains the  
76 decreased annular mode timescale during propagation relative to the stationary regime (Lubis  
77 and Hassanzadeh 2020). Further, the decorrelation timescales of both modes can be predicted  
78 across lags using knowledge only from a single lag in the propagating system (Sheshadri and  
79 Plumb 2017), which highlights the coupled dynamics of the modes.

80 Given the endurance of timescale biases across model generations (Gerber et al. 2008;  
81 Simpson and Polvani 2016; Bracegirdle et al. 2020), improving the representation of annular  
82 mode timescales will require capturing higher-order dynamics than those represented in dry,  
83 idealized models. For example, recent work has suggested that the presence of moisture acts  
84 variously as a positive feedback on annular modes by selectively damping high-frequency

85 eddies which shorten jet persistence (Lutsko and Hell 2021), or a negative feedback through the  
86 reduction of zonal-mean baroclinicity (Xia and Chang, 2014).

87         Beyond the effects of condensational heating, cloud radiative effects (CRE) have also  
88 been suggested to affect the annular mode timescale because high clouds respond to shifts in  
89 the Southern Hemisphere jet (Thompson and Wallace 2000, Liu et al. 2020). Yet it remains  
90 unclear how CRE might feedback on the annular modes. Li et al. (2014) suggest CRE might  
91 decrease the annular mode timescale in the Northern Hemisphere, but Papavasileiou et al.  
92 (2020) find CRE weakly increase the timescale of its regional manifestation, the North Atlantic  
93 Oscillation. Notably, Papavasileiou et al. (2020) find significant positive feedbacks from latent  
94 heating and clear-sky heating on the North Atlantic Oscillation.

95         Since diabatic heating can influence EOF1 variability, it suggests diabatic heating may  
96 also influence the propagation of annular mode anomalies. In idealized models, radiative  
97 damping of large-scale eddies is partially responsible for the meridional propagation of zonal  
98 wind anomalies (Lee et al. 2007). In this model, propagation is primarily a barotropic process  
99 driven by slow shifts in the critical latitude for wave breaking. However, other idealized models  
100 suggest a balance between baroclinic processes and radiative damping drive propagation  
101 (Sparrow et al. 2009). The relative contributions of baroclinic, barotropic, and diabatic  
102 processes to the propagation of annular mode anomalies have yet to be determined.

103         The relative balance between processes for stationary modes of variability is also  
104 unclear. Upper-level barotropic shifts feedback onto the low-level baroclinicity, which increases  
105 in response to surface friction and helps maintain the upper-level anomaly (Robinson 2000;  
106 Blanco-Fuentes and Zurita-Gotor 2011; Zurita-Gotor et al. 2014). Diabatic heating damps this

107 baroclinic response by modifying the low-frequency eddy forcing; suggesting an important but  
108 unclear role (Zurita-Gotor et al. 2014; Lutsko and Hell 2021). Nie et al. (2014; henceforth N14)  
109 attempt to resolve this using an eddy-mean flow interaction framework. However, their finding  
110 of primarily barotropic feedbacks neglects diabatic heating entirely, despite their framework's  
111 ability to quantify these impacts (Huang and Nakamura 2016).

112 The present work aims to address the following two questions. **First**, we seek to clarify  
113 the relative contributions of diabatic and other processes to the stationary regime in reanalysis  
114 data of the Southern Hemisphere, which has been the focus of many previous efforts to  
115 quantify eddy-jet feedbacks (Lorenz and Hartmann 2001; Simpson et al. 2013; N14) due to its  
116 relative zonal symmetry. **Second**, we examine the relative contributions of diabatic, baroclinic,  
117 and barotropic processes for the propagating regime of SAM variability. This further motivates  
118 examining SAM, as it exhibits both stationary and propagating regimes depending on the  
119 season (Sheshadri and Plumb, 2017; and Figure 1).

120 Using different seasons as proxies for stationary and propagating regimes of SAM, we  
121 apply the eddy-mean flow interaction framework of N14 to show that diabatic heating is the  
122 largest source of the eddy-jet feedback and the largest opposition to propagation in December-  
123 February (DJF). Additionally, baroclinic feedbacks, followed closely by diabatic feedbacks, are  
124 most important during March-November for the decorrelation timescale, while propagation is  
125 driven barotropically. Further, this work shows that the diabatic feedback in DJF is principally  
126 from clear-sky heating, while latent heating is more significant for the propagating regime in  
127 March-November. These diabatic feedbacks are likely are result of a shift in the latitude of

128 wave-breaking with the jet, resulting in warmer and wetter eddies for equatorward jet shifts  
129 and colder and drier eddies for poleward jet shifts.

130 The rest of the work is outlined as follows. We begin by reviewing the finite-amplitude  
131 wave activity (FAWA) theory which allows us to directly quantify the contributions of diabatic  
132 heating to the mean flow (Nakamura and Zhu 2010), highlighting where our analysis improves  
133 upon N14. We then outline our methodology based on the EMFC budget. The results of this  
134 budget are presented first, followed by an analysis of where and how diabatic feedbacks are  
135 operating. We conclude with some reflections on utilizing our methodology as a part of a  
136 strategy to determine the source of model biases.

137

## 138 **2. Theory**

139 A simple budget for SAM results from the vertically integrated, zonal-mean zonal  
140 momentum balance in quasi-geostrophy, projected onto SAM anomalies (Lorenz and  
141 Hartmann, 2001; N14):

$$142 \quad \frac{dz}{dt} = m_{\text{up}} - \frac{z}{D} \quad (1)$$

143 Where  $z$  is the principal component timeseries associated with SAM (zonal index) calculated  
144 from the full column,  $m_{\text{up}}$  is the projection timeseries for the upper-level EMFC,  $M$ , vertically  
145 integrated from 500-100hPa, and  $D$  is the damping timescale resulting from parameterizing  
146 boundary-layer drag as Rayleigh damping (Lorenz & Hartmann 2001). As in N14, we choose to  
147 focus on upper-level momentum because 1) the anomalous EMFC associated with SAM is  
148 concentrated above 500hPa, 2) SAM is understood as primarily barotropic, and 3) this division

149 enables us to separately understand contributions from the lower troposphere. The EMFC,  $M$ ,  
 150 is then given by

151

$$M \equiv -\frac{1}{a \cos^2 \phi} \frac{\partial}{\partial \phi} (\overline{u'v'} \cos^2 \phi),$$

152 Where the prime represents deviations from the zonal-mean (indicated by the overbar),  $\phi$  is  
 153 latitude,  $a$  is the planetary radius, and  $u$  and  $v$  are zonal and meridional velocity, respectively.

154 To further probe SAM dynamics, we make use of the FAWA framework for eddy-mean  
 155 flow interaction (Nakamura and Zhu 2010). FAWA is a contour integral transform of the quasi-  
 156 geostrophic (QG) potential vorticity (PV)  $q_g$ . FAWA ( $A$ ) measures the amplitude of large-scale  
 157 Rossby wave packets by integrating over the displacement of a PV anomaly from a conservative  
 158 zonal symmetry ( $Q$ )

159

$$A \equiv A^S + A^N \equiv \frac{a}{2\pi \cos \phi_e} \iint_{\substack{q > Q \\ \phi \leq \phi_e}} q_g \cos \phi d\lambda d\phi - \frac{a}{2\pi \cos \phi_e} \iint_{\substack{q \leq Q \\ \phi > \phi_e}} q_g \cos \phi d\lambda d\phi. \quad (2)$$

160 Here,  $\phi_e$  is the equivalent latitude, the latitude an anomaly would have in conservative zonal  
 161 symmetry.  $A^S$  and  $A^N$  are wave activity from southward contour displacements and northward  
 162 displacements, respectively. In the Southern Hemisphere,  $A^S$  is wave activity from large-scale  
 163 anticyclonic waves ( $q - Q > 0$ ), and  $A^N$  is from cyclonic waves ( $q - Q < 0$ ).

164 Applying the same integral transform in Eq. (2) to the PV budget results in a budget for  
 165 wave activity (c.f. N14; Nakamura and Solomon 2010; Palipane et al. 2017)

166

$$\frac{\partial A}{\partial t} = -\overline{v'_g q'_g} - K_{eff} \frac{1}{a} \frac{\partial Q}{\partial \phi} + \Delta \Sigma. \quad (3)$$

167 The subscript  $g$  indicates the geostrophic component of the wind,  $\Delta \Sigma$  represents diabatic and  
 168 nonconservative sources of wave activity, and  $K_{eff}$  is the effective diffusivity, representing the

169 small-scale destruction of PV through the stretching of the material PV contour.  $K_{eff}$  must be  
 170 diagnosed residually from Eq. (3).

171 Importantly, N14 assumes that  $\Delta\Sigma$  is negligible to compute  $K_{eff}$ , given that upper-  
 172 tropospheric diabatic heating is relatively small compared to lower-tropospheric diabatic  
 173 heating. However, we show that  $\Delta\Sigma$  is not negligible, as coincidence between diabatic heating  
 174 and upper-level wave breaking provides substantial opportunity for diabatic modulation of  
 175 wave activity, particularly when projected onto SAM. This has significant consequences for the  
 176 calculation of  $K_{eff}$  and the conclusions of N14, as we will show.

177 Making use of the equality between the meridional PV flux [first term on the rhs of Eq.  
 178 (3)] and Eliassen-Palm (EP) flux divergence in the QG framework, we can use Eq. (3) to develop  
 179 a budget for the geostrophic EMFC  $M_g$ , the geostrophic component of  $M$ ,

$$180 M = M_g + M_a = - \underbrace{\frac{\partial A}{\partial t}}_{\text{transient}} - f \underbrace{\frac{\partial}{\partial p} \left( \frac{\overline{v'_g \theta'}}{d\tilde{\theta}/dp} \right)}_{\text{baroclinic}} - \underbrace{K_{eff} \frac{1}{a} \frac{\partial Q}{\partial \phi}}_{\text{barotropic}} + \underbrace{\Delta\Sigma}_{\text{diabatic}} + M_a, \quad (4)$$

181 where  $M_a$  is the ageostrophic component of  $M$ . Eq. (4) represents the decomposition for the  
 182 EMFC into transient, barotropic, baroclinic, diabatic, and ageostrophic components. Note there  
 183 is a slight difference between N14's formulation of the baroclinic term, which utilizes the full  $v'$ ,  
 184 and ours, which utilizes only the geostrophic portion of  $v'$ . This allows for better understanding  
 185 of the contributions of the ageostrophic component, as we will show.

186 Diabatic contributions are found by applying the integral transform in Eq. (2) to the PV  
 187 source generated by the heating contributions (c.f. Andrews 1987, Palipane et al. 2017), or

$$188 \Delta\Sigma \equiv \frac{a}{2\pi \cos \phi_e} \left\{ \iint_{\substack{q > Q \\ \phi \leq \phi_e}} f \frac{\partial}{\partial p} \left[ \frac{(p_R p^{-1})^\kappa}{c_p d\tilde{\theta}/dp} J_T \right] \cos \phi d\lambda d\phi - \iint_{\substack{q \leq Q \\ \phi > \phi_e}} f \frac{\partial}{\partial p} \left[ \frac{(p_R p^{-1})^\kappa}{c_p d\tilde{\theta}/dp} J_T \right] \cos \phi d\lambda d\phi \right\} \quad (5)$$

189

190  $\kappa$  is the Poisson constant,  $c_p$  is the specific heat capacity at constant pressure,  $p_R = 1000 \text{ hPa}$   
191 is the reference pressure, and  $J_T \equiv J_{LH} + J_{CRE} + J_{CS}$  is the total diabatic heating rate, computed  
192 as the sum of individual heating rates due to condensation, cloud longwave and shortwave  
193 radiation, and clear-sky longwave and shortwave radiation. As with wave activity  $A$ ,  $\Delta\Sigma$  can be  
194 decomposed into cyclonic and anticyclonic contributions. Contributions are also computed  
195 individually for the heating rate for each process.

196 Vertically integrating Eq. (4) from 500-100 hPa and projecting onto SAM, we produce an  
197 expanded budget from Eq. (1) accounting for various physical processes

198 
$$m_{\text{up}} = m_A + m_{bt} + m_{bc} + m_{db} + m_{ag}. \quad (6)$$

199  $m_A$  are contributions from the (negative) wave activity tendency (i.e., the conservation of  
200 angular pseudomomentum),  $m_{bt}$  are contributions from large-scale barotropic mixing,  $m_{bc}$  are  
201 baroclinic contributions from the meridional eddy heat flux from the lower troposphere,  $m_{db}$   
202 are diabatic contributions, and  $m_{ag}$  are ageostrophic ones.

203 Finally,  $m_{db}$  can be further decomposed into various contributions as

204 
$$m_{db} \equiv m_{LH} + m_{LWCS} + m_{LWCRE} + m_{SWCRE} + m_{SWCS} \quad (7a)$$

205 
$$m_{db} \equiv m_{LH}^S + m_{LH}^N + m_{LWCS}^S + m_{LWCS}^N + m_{LWCRE}^S + m_{LWCRE}^N + m_{SWCRE}^S + m_{SWCRE}^N + m_{SWCS}^S + m_{SWCS}^N \quad (7b)$$

206 Here, subscripts on  $m$  denote contributions from latent heating (LH), longwave clear-sky  
207 heating (LWCS), longwave cloud radiative heating (LWCRE), shortwave clear-sky heating  
208 (SWCS), and shortwave cloud radiative heating (SWCRE). Superscripts denote diabatic  
209 contributions in anticyclonic waves (S) and cyclonic waves (N).

210

211    **3. Data/Methods**

212    *3.1. SAM Budget Analysis*

213         Following Simpson et al. (2013) and N14, we take the SAM indices as the first two EOFs  
214         of vertically-integrated, zonal-mean zonal wind, including the area-based weighting of EOFs  
215         (Baldwin et al. 2009). We then project the momentum budget onto each EOF spatial basis,  
216         regressing the terms onto the EOF timeseries. Decay timescales for each EOF are estimated by  
217         fitting an exponential curve to each autoregression. Lag-dependent timescales  $\tau$  are estimated  
218         assuming an exponential decay of the autoregression ( $C_{zz} \sim e^{-t/\tau}$ ) as  $\tau \sim -1/(d \ln C_{zz} / dt)^{-1}$   
219         after smoothing the derivative with a 7-point running mean (Zurita-Gotor et al. 2014).

220         Wave activity integrations described above are carried out through a careful, geo-  
221         located sorting of the PV field to find the zonally-symmetric reference PV, followed by a grid cell  
222         counting procedure to determine the displacement. Diabatic PV source fields are integrated  
223         over the same area, akin to the process for column-water vapor of Smith et al. (2021). PV  
224         source fields are computed using the integrand in Eq. (5) from diabatic heating rates taken  
225         directly from the reanalysis output (see section 3.3).

226         A composite of propagating events is made following a modification of the procedure  
227         outlined in Lee et al. (2007; see section 4.1). We identify middle times of candidate events as  
228         any time where zonal wind anomalies are a local maximum at 50 °S. Local maxima are identified  
229         as the maxima during a period beginning when the wind anomalies at 50 °S are greater than 1  
230         standard deviation above the mean and ending when anomalies have dipped below that value  
231         for at least three days. To remove propagation events who have anomalously short periods, the  
232         only local maxima retained must be a local maximum over a 70-day period centered on the

233 candidate maximum. The remaining local maxima are taken to be the middle times of  
234 propagating events, of which we identify 81.

235 Ninety-percent confidence intervals for each budget term are produced via  
236 bootstrapping. We generate 1000 random subsets of budget timeseries data (consecutively,  
237 with replacement) of length 2555 days (~7 years). All regressions are performed with each  
238 subset, selecting the 5<sup>th</sup> and 95<sup>th</sup> percentiles of the subsets as confidence interval bounds.

239 *3.2. Wave-breaking analysis*

240 We further investigate the physical mechanisms behind diabatic influences on SAM  
241 through an analysis of individual wave-breaking events. Wave-breaking events are identified  
242 here as regions above the 90<sup>th</sup> percentile for a given month in both cyclonic and anticyclonic  
243 wave activity separately, located between 25°-75°S. Identified regions must also be at least  
244 500,000 km<sup>2</sup> in size to remove small-scale contributions to wave activity.

245 Because FAWA measures *finite-amplitude* waves rather than simply linear waves, these  
246 large excursions of the PV contour from zonal symmetry are strongly nonlinear and generally  
247 correspond to wave breaking (Huang and Nakamura 2016; Nakamura and Huang 2017).

248 Notably, we do not impose a requirement for overturning of PV contours common to more  
249 traditional definitions, although upwards of 90% of the identified waves meet this definition  
250 (see Supplemental Figures 4 and 5). This interpretation of wave-breaking likely emphasizes the  
251 earlier stages of wave breaking over its more mature phases where strong mixing has returned  
252 the material PV contour closer to zonal symmetry. This latter irreversible destruction of PV is a  
253 sink of wave activity and captured in the barotropic term outlined in section 2.

254        After computing the center of mass of a large wave activity region, we interpolate all  
255    fields to a 3000 km x 3000 km locally Cartesian grid centered at the wave activity centroid  
256    (given in *equivalent* latitude) to capture the entire wave-breaking region. Fields are averaged  
257    over the domain and vertically from 500-100hPa for all identified wave breaking events, and  
258    then regressed against the year-round SAM (EOF1) index.

259        *3.3. Data Source*

260        Data for this work are obtained from NASA MERRA2 reanalysis. MERRA2 data are  
261    gridded at approximately 0.5° latitude by 0.625° longitude resolution, with 29 vertical levels  
262    between surface and mid-stratosphere (30hPa). Further details can be found in Gelaro et al.  
263    (2017). MERRA2 was chosen for this work because it provides different diabatic heating rates  
264    and fast accessibility. Due to storage constraints, a recent 15 years of 6-hourly data, 2005-2019,  
265    were selected. These high-frequency data are needed to resolve medium-scale waves (periods  
266    around 2 days) which contribute to SAM (Ma et al. 2017). Because we can identically reproduce  
267    N14's results, which utilized a different and longer dataset (see Supplemental Figure 1), we do  
268    not expect that our choice of dataset or temporal range are strongly impacting our results.

269        Data downloaded are horizontal velocity, geopotential height, temperature, surface  
270    pressure, and temperature tendencies due to longwave, longwave clear-sky, shortwave,  
271    shortwave clear-sky, and moist processes. Cloud heating rates are diagnosed simply as all-sky  
272    rates minus clear-sky rates.

273

274     **4. Results & Discussion**

275       *4.1. SAM Momentum Budgets*

276           We begin our discussion by recognizing that SAM exhibits different behavior in different  
277    seasons (Sheshadri and Plumb 2017; also Figure 1). MAMJJASON shows all the hallmarks of  
278    propagation: 1) cross-correlations between EOF1 and EOF2, 2) a similar decay timescale  
279    between EOFs 1 and 2, and 3) a similar fraction of variance explained by both EOFs (Lee et al.  
280    2007; Sheshadri and Plumb 2017; Lubis and Hassanzadeh 2020). In contrast, DJF shows: 1) weak  
281    cross-EOF correlations, 2) an EOF1 timescale almost double that of EOF2, and most importantly,  
282    3) more than twice the variance explained by EOF1 than by EOF2. [The threshold ratio for  
283    discriminating between regimes is 2:1, see Lee et al. (2007).] Physically, the stationary regime is  
284    associated with single jet climates when the eddy-driven jet is weak, such as during summer,  
285    and the propagating regime tends to form when the eddy-driven jet is stronger and displaced  
286    from the subtropical jet, as in most of the rest of the year (Lee et al. 2007). We proceed using  
287    DJF as a proxy for the stationary regime, and MAMJJASON as a proxy for the propagating  
288    regime. (Data are de-seasonalized before examining their relationship with SAM.)

289           The implied decorrelation timescale in Figure 1c,d (solid lines) demonstrates that the  
290    decorrelation timescale, often understood as constant (dashed lines), is only approximately so.  
291    The EOF1 decorrelation timescale peaks about day 9 in both seasons, while the EOF2  
292    decorrelation timescale peaks about day 12 (Figure 1c,d). Where these timescales are longer  
293    than SAM's frictional damping timescale of ~7-8 days, a positive feedback on the annular mode  
294    is implied (Lorenz and Hartmann 2001, Zurita-Gotor 2014, Lubis and Hassanzadeh 2020). Much  
295    of this analysis focuses on understanding relationships at lag day 10, a compromise between

296 the different peaks in feedbacks for EOFs 1 and 2 and the need to avoid the stochastic forcing  
297 of synoptic eddies at short timescales and the weak correlations at long lags.

298 Prior to lag day zero, SAM's EMFC for EOFs 1 and 2 for both seasons is primarily  
299 barotropic and transient (Figure 2a,b), consistent with N14 and expectation (Thompson and  
300 Wallace 2000). The MERRA2 budget is well-closed (compare black, dashed line with black solid  
301 line in Figure 2), and it compares favorably with Simpson et al. (2013) and N14 (see  
302 Supplemental Figure 1 for more details), confirming the validity of our assumptions outlined in  
303 section 2. The barotropic nature of the propagating regime stands out, where almost the entire  
304 peak around lag day -1 comes from  $m_A$  and  $m_{bt}$  for both EOFs.  $m_A$  represents transient  
305 fluctuations in Rossby wave growth, whose amplitude grows proportionally at the expense of  
306 the mean flow (Nakamura and Zhu 2010; Wang and Nakamura 2015). This partitioning  
307 underscores previous work that SAM's existence is essentially barotropic (N14, Thompson and  
308 Wallace 2000), although this extends to the pulsating variability (EOF2). Diabatic heating  
309 provides positive but smaller contributions to the generation of EOFs 1 and 2 (lead days -5 to 0),  
310 although it contributes substantially to the generation of EOF2 in DJF.

311 At positive lags, both seasons suggest an eddy-jet "feedback", evinced by positive  
312 correlations of the EMFC with the SAM at lag days 8-12 (Figure 1c,d; Lorenz and Hartmann  
313 2001; Simpson et al. 2013). The feedback in DJF is larger than in MAMJJASON, which could be  
314 attributed to stratospheric influence (Byrne et al. 2016; Saggioro and Shepherd 2019). Another  
315 (and not mutually exclusive) possibility is that stationary EOFs have longer EOF1 timescales;  
316 faster propagation in MAMJJASON could be reducing the persistence (Lubis and Hassanzadeh  
317 2020).

318        Regardless of the distal cause, the SAM eddy-jet feedback in MERRA2 is proximately due  
319    to diabatic heating and the eddy heat flux (Figure 2). For the stationary regime, the diabatic  
320    term is the largest positive contributor to the budget for lag days 0-20 (Figure 2a). For the  
321    propagating regime, the baroclinic term is the largest positive contributor for lag days 2-4, but it  
322    has parity with the diabatic term for lag days 5-15 (Figure 2b). EOF2 has similar relationships,  
323    where the diabatic term is the largest positive term for most lags shown here for the stationary  
324    regime, and on par with the baroclinic term for days 0-10 for the propagating regime.

325        A consequence of the importance of diabatic heating is the overestimation of barotropic  
326    effects by N14, who implicitly combine the two. Figure 2 shows barotropic mixing largely damps  
327    EOF 1 and 2 at positive lags in all seasons. N14 also neglect ageostrophic effects, but  
328    quantifying them (c.f. Eq. 4) reveals their magnitude is about half of the EMFC's at lag days 8-12  
329    for EOF1 (Figure 2a,b). This implies contributions to persistence from an ageostrophic mean  
330    meridional circulation, also found in idealized models (Son and Lee 2006; Zurita-Gotor et al.  
331    2014).

332        To interpret the cross-EOF momentum budget, we must determine the period of  
333    propagation and choose the arbitrary signs for the EOFs. Here, we choose signs such that  
334    progression from positive EOF1 to positive EOF2 to negative EOF1 to negative EOF2 represents  
335    poleward propagation. The period is about 60 days, determined by compositing the  
336    propagation events detected using the scheme outlined in section 3.2, whose results are shown  
337    in Figure 3e. The 60-day period suggested by the compositing analysis is supported by a strong  
338    peak in the EOF1 power spectrum at around 60 days (not shown), and it is consistent with  
339    earlier, observationally based estimates of meridional propagation (Riehl et al. 1950; Feldstein

340 1998). Thus, where an EOF2 momentum source is positively correlated with EOF1 within 15  
341 days of EOF1's peak, that momentum source is driving poleward propagation, and similarly but  
342 oppositely for EOF1 momentum sources. All of this is captured by the grey shaded regions in  
343 Figure 3a-d. Note that the EMFC (black lines in Figure 3) is roughly consistent with poleward  
344 propagation at all lags in both seasons.

345 From the budget for cross-EOF interaction, the barotropic term clearly initiates the  
346 poleward propagation (pink lines in Figure 3a-d). This is consistent with the wave-breaking  
347 propagation mechanism of Lee et al. (2007) found in an idealized dry model, but, to the best of  
348 the authors' knowledge, it has not been confirmed in reanalysis until this work. Consistent with  
349 our interpretation of MAMJJASON as the propagating season, the barotropic driver in the  
350 propagating regime is nearly twice as strong as it is during DJF. However, it is clear there is still  
351 some propagation during DJF, despite it being weaker. The composite analysis confirms the  
352 presence of propagation in DJF with 18 of the 81 middle times being in austral summer. DJF  
353 also exhibits stronger barotropic driving than MAMJJASON at positive lags greater than 15 days.

354 While the barotropic contributions initiate propagation, it is sustained baroclinically in  
355 response to the barotropic anomalies (red lines in Figure 3). Upon inspection, barotropic and  
356 baroclinic forcings tend to "see-saw". First, the barotropic is a poleward forcing while the  
357 baroclinic is equatorward, then they switch so that the baroclinic term is the dominant  
358 poleward forcing and the barotropic is equatorward around lag days 1-10. By lag day 15, a  
359 quarter of a period, the barotropic is again poleward and the baroclinic is equatorward. This  
360 kind of cancellation between the barotropic and baroclinic responses of SAM have been well-

361 documented at short timescales and gives some confidence in our interpretation (Boljka et al.  
362 2018; also Sparrow et al. 2009; Zurita-Gotor et al. 2014).

363 If propagation is initiated by barotropic momentum sources and sustained by baroclinic  
364 ones, it is primarily opposed by diabatic heating. Diabatic heating from one EOF is generally the  
365 same sign as the prior barotropic and baroclinic peaks, but it peaks too late (day 15-20) to aid  
366 transition to the other EOF (orange lines in Figure 3). Rather diabatic forcing appears in  
367 quadrature with the EMFC anomalies, consistent with its increasing of persistence seen in the  
368 separate EOF budgets (Figure 2). Interestingly, most of this equatorward forcing from diabatic  
369 heating comes from the latent heating (see Supplemental Figure 3), whose introduction in  
370 idealized models can in some cases trigger propagation (Lutsko and Hell 2021). This diabatic  
371 drag on propagation is strongest in the stationary regime where propagation is weakest (Figure  
372 3a), where the diabatic feedback on EOFs 1 and 2 is also strongest (Figure 2a,c). Ageostrophic  
373 momentum also appears to oppose propagation (brown lines in Figure 3) and increase  
374 persistence (Figure 2), suggesting that the slower response of these processes to EOF anomalies  
375 may favor slower propagation and enhanced persistence.

376 Additionally, the barotropic term in Figure 3b,d appears to be responsible for the poor  
377 budget closure between lag day -8 and 0 (comparing black, dashed line to black, solid line).  
378 Because the barotropic term is computed residually, the only possible source of error  
379 (excluding numerical, which the strong budget closure in Figure 2 suggests is unlikely) would be  
380 the QG approximation that the meridional PV flux balances the EP flux divergence, implying  
381 some of the interactive PV flux is being dissipated at non-QG scales. Because the dissipation of

382 the eddy PV forcing has a strong control over the resulting SAM dynamics (Zurita-Gotor et al.  
383 2014), this result requires further investigation outside the scope of this work.

384 We now examine where momentum is being produced by each mechanism to gain  
385 more physical insight (Figure 4). At a 10-day lag, diabatic momentum for EOF1 during DJF is  
386 concentrated poleward of the jet, decelerating the zonal wind there during the equatorward  
387 phase of SAM (positive EOF1; orange line in Figure 4a), in-phase with the EMFC anomalies  
388 (black line). Baroclinic momentum generation (red line) is the dominant term equatorward of  
389 the jet for EOF1, appearing on the poleward edge of the equatorward EMFC peak (black line).  
390 However, there is no clear shift in the EMFC (solid black line) that would suggest propagation,  
391 rather the pattern is one of reinforcement for EOF1 (thick grey line), consistent with a positive  
392 feedback. Barotropic (pink) and ageostrophic (brown) effects largely cancel one another.

393 Looking at EOF2 during DJF, the EMFC has flipped to a negative EOF2 pattern at a 10-day  
394 lag, further supporting DJF as the stationary regime (Figure 4c). Diabatic deceleration is  
395 confined poleward of the jet, as with EOF1. Baroclinic processes (red line) are also concentrated  
396 poleward of the jet, shifted poleward compared to EOF1 (Figure 4a). However, these diabatic  
397 and baroclinic sources are largely balanced by a growth in wave activity on the poleward jet  
398 flank (dashed blue line in Figure 4c). The negative EOF2 pattern of the EMFC appears to be  
399 generated most strongly by the barotropic piece. Thus, wave breaking acts to slow the jet  
400 during EOF2 in the stationary regime.

401 For the propagating regime at a 10-day lag, we see evidence of propagation in the  
402 EMFC, as expected, with diabatic and baroclinic forcings behaving similarly to the stationary  
403 regime (Figure 4b,d). The baroclinic term is shifted slightly further poleward for EOF1 than in

404 DJF, resulting in a positive EOF2-like pattern (Figure 4b). This shifting of the baroclinic term,  
405 combined with more negative diabatic contributions equatorward of the jet, results in an  
406 overall weaker positive EOF1 pattern for the EMFC (black line) and thus a weaker feedback than  
407 for DJF. Poleward of the jet, the diabatic term is balanced by the more positive barotropic term.  
408 The barotropic term has a negative EOF1-like response on the poleward edge of the positive  
409 EOF2-like baroclinic response, consistent with the barotropically initiated – baroclinically  
410 sustained pattern for propagation.

411 The EOF2 EMFC during MAMJJASON (Figure 4d) shows a clear negative EOF1 pattern  
412 (c.f. gray shading in Figure 4b) at a 10-day lag, evidence of poleward propagation. Despite this,  
413 the diabatic, barotropic, and baroclinic terms largely resemble the stationary regime. Diabatic  
414 and baroclinic sources are again primarily contributing poleward of the jet, and the barotropic  
415 term is a negative EOF2-like response, in quadrature with the EMFC and consistent with its  
416 initiation of propagation. Combined with diabatic and baroclinic effects, these generate the  
417 negative EOF1 which sustains the propagation. This highlights the careful synchronization  
418 between diabatic heating, upper-level wave growth, and lower-level eddy-heat flux required for  
419 propagation (Lee et al. 2007). Diabatic contributions are further examined in section 4.2.

420

#### 421 *4.2. SAM Diabatic Momentum Sources*

422 As discussed in section 2, diabatic momentum is the sum of momentum from several  
423 heating sources. We now separately consider diabatic contributions from latent heating, long-  
424 and short-wave clear-sky radiative heating, and long- and short-wave cloud radiative heating.  
425 Shortwave contributions (shown in Supplemental Figure 2) are found to be generally opposing

426 longwave contributions, but they are an order of magnitude smaller. Thus, while included in the  
427 total contributions, we neglect them for the remainder of this analysis.

428       The process-level decomposition reveals different processes dominate at different  
429 timescales (Figure 5). On short timescales less than  $\pm 10$  days, latent heating is generally the  
430 largest positive contributor to SAM momentum among the diabatic terms for EOF1 in both  
431 seasons (solid teal lines in Figure 5a,b), as well as for EOF2 in MAMJJASON. In general, much of  
432 the temporal structure in both regimes also comes from latent heating. Consistent with Lutsko  
433 and Hell (2021), we find latent heating is a positive feedback on SAM persistence. While this  
434 may seem at odds with Xia and Chang (2014), who argue for a negative latent heating feedback,  
435 this eddy-interaction framework does not consider indirect diabatic contributions from the  
436 adjustment of low-level baroclinicity, which are instead included in the baroclinic term.

437       While the role of latent heating is generally consistent across regimes, clear-sky  
438 momentum contributions primarily explain the difference between stationary and propagating  
439 regimes (solid purple lines in Figure 5). The clear-sky forcing is exclusively positive, with a  
440 magnitude ranging from 2-5 times larger during DJF than during MAMJJASON (Figure 5).  
441 Because clear-sky contributions are the dominant diabatic contributions beyond lag day 10 in  
442 DJF (Figure 5a), and because diabatic terms are the largest positive contributions for the entire  
443 budget (Figure 2a), clear-sky heating explains much of the increased persistence of the  
444 stationary regime.

445       While clear-sky and latent heating dominate at their respective timescales, cloud  
446 radiative heating is a second-order contributor to SAM dynamics (solid grey lines in Figure 5).  
447 This is likely a result of the relatively weak cloud response and complex vertical structure of the

448 cloud heating (Li and Thompson, 2016). However, despite being a small momentum source, it is  
449 the only term to clearly change sign over time in EOF1. At leads -10 to around lag day 2, cloud  
450 contributions are negative, damping the generation of EOF1 in both seasons (Figure 5a,b). At  
451 around lag day 3, the cloud contributions change sign, peaking around lag day 8 in the  
452 propagating case (Figure 5b), weakly increasing SAM persistence.

453 Further breaking the momentum into separate contributions from cyclonic and  
454 anticyclonic waves, nearly all the positive forcing comes from anticyclonic waves (dashed lines  
455 in Figure 5). Cyclonic wave sources for clear-sky heating (dotted purple) and cloud heating  
456 (dotted grey) damp the EMFC for SAM in all seasons for all EOFs. For clear-sky heating, the total  
457 momentum contributions exhibit a large degree of competition between anticyclonic  
458 contributions, peaking between 1.5-2 m/s/day, and cyclonic contributions, peaking between 1-  
459 1.5 m/s/day. Similar cancellation can be seen for cloud radiative heating for most seasons and  
460 EOFs, except for EOF2 during DJF, where both contributions hover around 0.

461 Interestingly, the cyclonic momentum contributions from clouds (dotted grey lines in  
462 Figure 5) almost entirely cancel those from latent heating (dotted teal) for most seasons and  
463 EOFs, again excepting DJF EOF2. This pattern does not hold for anticyclonic contributions,  
464 where cloud and latent heating sources are generally both positive. Latent heating is the only  
465 term that does not generally see competition between cyclonic and anticyclonic contributions,  
466 perhaps explaining why it drives diabatic contributions at short timescales.

467 We have already shown that diabatic contributions at a 10-day lag are concentrated  
468 poleward of the jet (Figure 4), but further analysis reveals that diabatic momentum for EOF1 is  
469 concentrated in the mid-troposphere between 500-300hPa (Figure 6). For the stationary

470 regime, latent heating broadly reinforces the peak-day EMFC anomaly (contour lines), in-phase  
471 with the anomaly on both flanks of the jet and still at nearly half of the magnitude of the peak  
472 EMFC ten days later (Figure 6a). This is likely from an equatorward shift of the storm tracks, as  
473 we show in section 4.3. During the propagating regime, latent heating is also in-phase around  
474 500hPa poleward of the jet, somewhat weaker than during the stationary mode (Figure 6b).

475 The radiative contributions from cloud and clear-sky heating are less in-phase with the  
476 EMFC anomalies than latent heating, and they are mostly concentrated below 200hPa. Cloud  
477 radiative heating is weakly in-phase with EMFC anomalies poleward of the jet for both seasons  
478 (Figure 6c,d). Cloud contributions have the most vertical variation of the diabatic terms, in-  
479 phase with the EMFC anomalies in some regions while out-of-phase in others. Because there is  
480 great uncertainty in SAM's influence of the vertical profile of cloud heating and the net impact  
481 results from a vertical average (Li and Thompson, 2016), cloud contributions may still  
482 contribute to model biases in annular mode timescale despite their small magnitude.

483 Clear-sky momentum sources exhibit the most variation of all the diabatic sources for  
484 EOF1 (Figure 6e,f). Clear-sky forcing during the stationary regime is well-aligned with the EMFC  
485 anomalies, with deceleration poleward of the jet extending into the lower stratosphere (Figure  
486 6e). In contrast, the propagating regime exhibits approximately 50% weaker clear-sky influence  
487 and is generally less in-phase with the EMFC poleward of 50°S (Figure 6f). This result could  
488 support proposals for a stratospheric influence on EOF1 during DJF (Byrne et al. 2016, Saggioro  
489 and Shepherd 2019), if stratospheric temperature anomalies are modifying upper-tropospheric  
490 longwave radiation. Further investigation for a radiative pathway for stratospheric influence is  
491 left for future work.

492 When looking at the spatial structure of diabatic momentum for EOF2, we see mostly  
493 reinforcement of the EOF2 EMFC pattern at a 10-day lag (Figure 7). This is particularly the case  
494 for latent and cloud radiative heating, which provide momentum sources reinforcing the  
495 stronger jet in the mid-troposphere in all seasons (Figure 7a-d). In both seasons, the cloud  
496 contributions to EOF2 (Figure 7c,d) are mostly opposite sign to their EOF1 contributions (Figure  
497 6c,d), still exhibiting the most vertical cancellation. Clear-sky heating projects weakly onto  
498 EOF2, largely within -0.1 to 0.1 m/s/day. During the propagating regime, clear-sky contributions  
499 (Figure 7f) are a weak negative EOF1-like pattern (cf. Figure 6f), but this is unlikely to be  
500 supporting propagation considering the previous analysis. In section 4.3, we analyze wave-  
501 breaking regions to identify physical mechanisms for the diabatic feedbacks and to investigate  
502 the role of anticyclonic and cyclonic circulation interactions.

503

#### 504 *4.3. Wave-breaking Analysis*

505 As described in section 3.2, the final part of this analysis tracks regions of upper-level  
506 large-scale cyclonic wave-breaking (CWB) and anticyclonic wave-breaking (AWB) to detect  
507 consistent trends between physical drivers of diabatic heating and the heating's impact on  
508 momentum. This provides some insight into probable mechanisms through which changes in jet  
509 latitude (the EOF1 mode) might lead to the diabatic feedbacks described in the previous  
510 section. We focus on large-scale wave breaking regions because they are the largest  
511 contributors to wave activity (Nakamura and Huang 2017), and because wave breaking in  
512 different phases of SAM contributes to asymmetries in its timescale (Barnes et al. 2010).

513            We examine correlations between EOF1 and wave breaking regimes at a 10-day lag,  
514   both poleward of the jet (50°-70°S) and equatorward of the jet (30°-50°S). We make this  
515   distinction for two reasons. First and foremost, the EMFC has different signs on opposite sides  
516   of the jet (approximately 50°S), and so a positive diabatic forcing may reinforce or oppose this  
517   pattern depending on its latitude (as suggested by the plus/minus signs in Figures 8-10).  
518   Second, the distributions of these fields are quasi-bimodal, and they are more Gaussian if first  
519   separated by latitude (not shown). Since we might reasonably expect similar diabatic responses  
520   to EOF1 regardless of the regime, we focus our efforts on year-round data to help improve the  
521   signal against the noisiness of synoptic-scale weather systems.

522            Consistent with previous regressions (Figure 6d), the positive longwave (LW) cloud  
523   feedback seen in Figure 5b is primarily coming from decreases in the cloud momentum source  
524   in both poleward AWB (PAWB) regions and CWB regions (PCWB; Figure 8a,b). This decreased  
525   momentum source is accompanied by a consistent weakening of upper-level cloud LW cooling  
526   (negative heating) in both poleward regions, along with decreases in upper-level humidity and  
527   cloud fraction. Physically, this suggests this diabatic feedback may be due to a reduced cloud  
528   fraction resulting from an upper-level drying in response to the more equatorward jet.

529            The effects of heating on PV depend on the vertical profile of the heating (c.f. Eq. (5)),  
530   and so changes (or lack thereof) in the vertically-averaged heating do not directly imply changes  
531   in PV. Even so, there is a reduction of the cloud cyclonic PV generation for PCWB (Figure 8b)  
532   and a weak increase in the cloud anticyclonic PV source for PAWB (Figure 8a), which we might  
533   expect given that cloud LW cooling weakens similarly in both regions.

534            Looking at equatorward AWB (EAWB), there are few significant relationships between  
535    SAM and these cloud-related variables (Figure 8c). There are no significant changes to the  
536    dynamical measures in equatorward CWB (ECWB) regions as well, though we do see a robust  
537    increase in cloud LW cooling coincident with increased cloud fraction, opposite the response in  
538    poleward regions (Figure 8d). Given the negative cloud momentum anomalies between 30°-  
539    50°S in Figure 6d, it is likely there is a weak negative feedback in the equatorward regions that  
540    is difficult to identify amidst the noise. However, the momentum budget (Figure 5b) shows this  
541    negative feedback in equatorward regions is weaker than the positive one in poleward regions.

542            Changes in clear-sky heating momentum are similarly positive in poleward regions,  
543    where an equatorward jet is linked to more equatorward and thus warmer wave breaking for  
544    PAWB, PCWB, and EAWB regions (Figure 9a-c). The warmer temperatures coincide with  
545    increased longwave cooling in all these regions as well as increased anticyclonic PV generation  
546    or cyclonic PV damping (Figure 9a-c). This suggests the positive clear-sky feedback comes from  
547    the equatorward shift of the storm tracks, producing increased longwave cooling in poleward  
548    waves, strengthening AWB and weakening CWB.

549            Interestingly, ECWB shows opposite trends to the other regions (Figure 9d). Here, we  
550    see a decrease in the momentum source, implying a negative feedback. This is consistent with a  
551    counter-intuitive shift towards higher latitude CWB (during equatorward SAM), a reduction in  
552    temperature, and a weakening of clear-sky cooling (Figure 9d). Our previous results suggest  
553    that SAM's clear-sky heating generates momentum equatorward of the jet (Figures 5b and 6f),  
554    so this reduction would imply that wave breaking only mediates some of the diabatic impacts.  
555    In other words, the lower nine deciles of wave activity may provide this positive feedback,

556 countervailing the changes seen in this top decile. Another consideration is the fact that we are  
557 tracking equivalent latitudes, and that, somewhat paradoxically, AWB tends to be identified at  
558 higher equivalent latitudes than CWB (Supplemental Figure 6).

559 To conclude this analysis, we examine fields relevant to latent heating at a 10-day lag,  
560 which also support a feedback due to the shift in storm tracks (Figure 10). As with the clear-sky  
561 fields, the equatorward shift in cyclones and anticyclones result in more moisture availability  
562 and stronger latent heating in PAWB, PCWB, and EACWB regions (Figure 10a-c). This  
563 diabatically-driven persistence of storm track shifts is consistent with observational studies of  
564 the North Atlantic basin (Woollings et al. 2016). Where the latent heating increase is robust  
565 (PCWB, EAWB), it strengthens AWB and weakens CWB, acting as a positive feedback, consistent  
566 with Figures 6b and 5b. The most robust changes are seen for PCWB, where cyclones shift more  
567 equatorward, and thus have more moisture available for latent heating (Figure 10b).

568 Similar to the clear-sky response, the pattern is reversed for ECWB regions: more  
569 poleward cyclones, with less moisture available and mildly weaker latent heating (Figure 10d).  
570 While the changes to CWB equatorward of the jet during SAM are not consistent with the other  
571 regions, they are internally consistent, suggesting that this analysis does identify the relevant  
572 physical mechanisms which are mediating the diabatic feedbacks on SAM. Thus, 10 days after  
573 peak SAM, storm tracks are still displaced, modifying the latent and clear-sky heating in such a  
574 way as to increase SAM persistence.

575

576     **5. Conclusions**

577         To quantify the contributions of diabatic, barotropic, and baroclinic processes to the  
578         persistence and propagation of SAM, we have examined a detailed budget for the EMFC in  
579         MERRA2 from 2005-2019. Principally, we find that diabatic heating, particularly from latent and  
580         longwave clear-sky heating, is the dominant source of momentum at positive lags during DJF,  
581         for both the jet shift (EOF1) and jet pulsing (EOF2) modes of variability. Thus, diabatic effects  
582         constitute the largest eddy-jet feedback for the stationary regime of SAM variability. This is a  
583         novel contribution of this work which corrects the earlier work of N14.

584         Because diabatic heating is the largest feedback during DJF, and because this feedback is  
585         tied to the latitude of wave breaking and thus the jet itself, efforts to improve representation of  
586         SAM in models should first consider the climatological jet latitude. However, improved  
587         climatological jet latitudes have not eliminated DJF timescale biases in CMIP6 (Bracegirdle et al.  
588         2020), and these results urge further consideration of whether the often-parameterized  
589         diabatic processes in models generate a realistic vertical profile of heating in response to SAM.  
590         Additionally, our results imply dry models will not properly simulate SAM timescales.

591         For the propagating regime of SAM variability during March-November, we find  
592         baroclinic contributions from the meridional eddy heat flux are the largest source of EOF1 and  
593         EOF2 momentum at positive lags, followed closely by diabatic heating. Additionally, barotropic  
594         contributions initiate the EOF1-EOF2 interaction which drives poleward propagation, which is  
595         supported by a baroclinic response. Diabatic heating generally opposes poleward propagation,  
596         consistent with the finding that it increases persistence (Lubis and Hassanzadeh 2020).

597        Additionally, diabatic heating may explain the tendency towards a stationary regime in  
598 DJF through a stronger clear-sky momentum source and a stronger damping of propagation  
599 than in MAMJJASON. More fundamentally, the tendency towards propagation or non-  
600 propagation has been explained as result of double or single jet states (Lee et al 2007), the  
601 latter being more common in summer due to the weakened eddy-driven jet. These mechanisms  
602 are not mutually exclusive – jet latitude has an important influence over diabatic heating. These  
603 results for the propagating regime highlight the careful orchestration between processes  
604 required to produce an accurate SAM timescale and thus to predict SAM evolution. Future  
605 progress relies on identifying the controls on the speed of propagation and quantifying  
606 momentum budgets in full-physics models.

607        Some of the authors have already begun quantifying SAM EMFC budgets in a suite of  
608 “cloud-locking” experiments in the Exascale Energy Earth System Model (E3SM) designed to  
609 eliminate cloud-circulation feedbacks (Brice Harrop, personal communication). Similar methods  
610 to this work will further probe the interaction between cloud heating and SAM. Of particular  
611 interest is whether modeled cloud-SAM feedbacks are stronger than those seen in this work for  
612 MERRA2, which found them to be relatively weak but likely positive.

613        A final caveat is suggested by the results of Chemke and Polvani (2019), who argue that  
614 discrepancies between reanalyses and models sometimes represent deficiencies in the  
615 reanalyses and not the models, as in the case of trends in Hadley cell strength. While this  
616 analysis cannot definitively demonstrate the validity of these results beyond MERRA2, this work  
617 is internally consistent and broadly in agreement with modeling studies, suggesting that our key  
618 findings on the importance of diabatic heating for SAM are likely not a result of artefacts.

619 Our approach taken here elucidates many different facets controlling the variability of  
620 the Southern Hemisphere zonal wind. We find diabatic heating is crucial to setting the  
621 timescale of a largely barotropic phenomena. We also find consistencies between reanalysis  
622 and idealized modeling studies, increasing our confidence that mechanisms operating in the  
623 idealized studies are also operating in the real atmosphere. We contend that coupling this  
624 budget-based approach with targeted model experiments could be an ideal strategy for  
625 determining the underlying controls for a host of annular mode behaviors.

626

### 627 **Acknowledgements**

628 We acknowledge NASA for its provision of MERRA2 data. Python libraries Numpy,  
629 matplotlib, and xarray expedited the analysis and visualization. This research was partially  
630 supported by Lilly Endowment, Inc., through its support for the Indiana University Pervasive  
631 Technology Institute. S.S. is supported under NASA FINESST Award 80NSSC21K1596, P.S. under  
632 NSF Grant 1813981, and J.L. by the DOE Office of Science Biological and Environmental  
633 Research as part of the Regional and Global Modeling and Analysis program area.

634

### 635 **Data Availability Statement**

636 MERRA2 data is publicly available from NASA GES DISC (DOI: 10.5067/A7S6XP56VZWS;  
637 10.5067/9NCR9DDDOPFI). Code for computing the local wave activity budget is available from  
638 the corresponding author upon request.

639 References

- 640 Andrews, D. G., 1987: *Middle atmosphere dynamics*. J.R. Holton and C.B. Leovy, Eds. Academic  
641 Press.

642 Baldwin, M. P., and T. J. Dunkerton, 2001: Stratospheric Harbingers of Anomalous Weather  
643 Regimes. *Science*, **294**, 581–584, <https://doi.org/10.1126/science.1063315>.

644 ——, D. B. Stephenson, and I. T. Jolliffe, 2009: Spatial Weighting and Iterative Projection  
645 Methods for EOFs. *Journal of Climate*, **22**, 234–243,  
646 <https://doi.org/10.1175/2008JCLI2147.1>.

647 Barnes, E. A., D. L. Hartmann, D. M. W. Frierson, and J. Kidston, 2010: Effect of latitude on the  
648 persistence of eddy-driven jets. *Geophysical Research Letters*, **37**,  
649 <https://doi.org/10.1029/2010GL043199>.

649 Blanco-Fuentes, J., and P. Zurita-Gotor, 2011: The driving of baroclinic anomalies at different  
650 timescales. *Geophysical Research Letters*, **38**, <https://doi.org/10.1029/2011GL049785>.

651 Boljka, L., T. G. Shepherd, and M. Blackburn, 2018: On the Coupling between Barotropic and  
652 Baroclinic Modes of Extratropical Atmospheric Variability. *Journal of the Atmospheric  
653 Sciences*, **75**, 1853–1871, <https://doi.org/10.1175/JAS-D-17-0370.1>.

654 Bracegirdle, T. J., C. R. Holmes, J. S. Hosking, G. J. Marshall, M. Osman, M. Patterson, and T.  
655 Rackow, 2020: Improvements in Circumpolar Southern Hemisphere Extratropical  
656 Atmospheric Circulation in CMIP6 Compared to CMIP5. *Earth and Space Science*, **7**,  
657 e2019EA001065, <https://doi.org/10.1029/2019EA001065>.

- 659 Byrne, N. J., T. G. Shepherd, T. Woollings, and R. A. Plumb, 2016: Annular modes and apparent  
660 eddy feedbacks in the Southern Hemisphere. *Geophysical Research Letters*, **43**, 3897–  
661 3902, <https://doi.org/10.1002/2016GL068851>.
- 662 Chemke, R., and L. M. Polvani, 2019: Opposite tropical circulation trends in climate models and  
663 in reanalyses. *Nat. Geosci.*, **12**, 528–532, <https://doi.org/10.1038/s41561-019-0383-x>.
- 664 Feldstein, S. B., 1998: An Observational Study of the Intraseasonal Poleward Propagation of  
665 Zonal Mean Flow Anomalies. *Journal of the Atmospheric Sciences*, **55**, 2516–2529,  
666 [https://doi.org/10.1175/1520-0469\(1998\)055<2516:AOSOTI>2.0.CO;2](https://doi.org/10.1175/1520-0469(1998)055<2516:AOSOTI>2.0.CO;2).
- 667 Gelaro, R., and Coauthors, 2017: The Modern-Era Retrospective Analysis for Research and  
668 Applications, Version 2 (MERRA-2). *J. Climate*, **30**, 5419–5454,  
669 <https://doi.org/10.1175/JCLI-D-16-0758.1>.
- 670 Gerber, E. P., L. M. Polvani, and D. Ancukiewicz, 2008: Annular mode time scales in the  
671 Intergovernmental Panel on Climate Change Fourth Assessment Report models.  
672 *Geophysical Research Letters*, **35**, <https://doi.org/10.1029/2008GL035712>.
- 673 Gritsun, A., and G. Branstator, 2007: Climate Response Using a Three-Dimensional Operator  
674 Based on the Fluctuation–Dissipation Theorem. *Journal of the Atmospheric Sciences*, **64**,  
675 2558–2575, <https://doi.org/10.1175/JAS3943.1>.
- 676 Hassanzadeh, P., and Z. Kuang, 2016: The Linear Response Function of an Idealized  
677 Atmosphere. Part II: Implications for the Practical Use of the Fluctuation–Dissipation  
678 Theorem and the Role of Operator’s Nonnormality. *Journal of the Atmospheric Sciences*,  
679 **73**, 3441–3452, <https://doi.org/10.1175/JAS-D-16-0099.1>.

- 680 Huang, C. S. Y., and N. Nakamura, 2016: Local Finite-Amplitude Wave Activity as a Diagnostic of  
681 Anomalous Weather Events. *Journal of the Atmospheric Sciences*, **73**, 211–229,  
682 <https://doi.org/10.1175/jas-d-15-0194.1>.
- 683 Kidson, J. W., 1988a: Indices of the Southern Hemisphere Zonal Wind. *Journal of Climate*, **1**,  
684 183–194, [https://doi.org/10.1175/1520-0442\(1988\)001<0183:IOTSHZ>2.0.CO;2](https://doi.org/10.1175/1520-0442(1988)001<0183:IOTSHZ>2.0.CO;2).
- 685 ——, 1988b: Interannual Variations in the Southern Hemisphere Circulation. *Journal of Climate*,  
686 **1**, 1177–1198, [https://doi.org/10.1175/1520-0442\(1988\)001<1177:IVITSH>2.0.CO;2](https://doi.org/10.1175/1520-0442(1988)001<1177:IVITSH>2.0.CO;2).
- 687 Kidston, J., and E. P. Gerber, 2010: Intermodel variability of the poleward shift of the austral jet  
688 stream in the CMIP3 integrations linked to biases in 20th century climatology.  
689 *Geophysical Research Letters*, **37**, <https://doi.org/10.1029/2010GL042873>.
- 690 Lee, S., and S. Feldstein, 1996: Mechanism of Zonal Index Evolution in a Two-Layer Model.  
691 *Journal of the Atmospheric Sciences*, **53**, 2232–2246, [https://doi.org/10.1175/1520-0469\(1996\)053<2232:MOZIEI>2.0.CO;2](https://doi.org/10.1175/1520-0469(1996)053<2232:MOZIEI>2.0.CO;2).
- 693 ——, S.-W. Son, K. Grise, and S. B. Feldstein, 2007: A Mechanism for the Poleward Propagation  
694 of Zonal Mean Flow Anomalies. *Journal of the Atmospheric Sciences*, **64**, 849–868,  
695 <https://doi.org/10.1175/JAS3861.1>.
- 696 Li, Y., and D. W. J. Thompson, 2016: Observed Signatures of the Barotropic and Baroclinic  
697 Annular Modes in Cloud Vertical Structure and Cloud Radiative Effects. *Journal of  
698 Climate*, **29**, 4723–4740, <https://doi.org/10.1175/JCLI-D-15-0692.1>.
- 699 ——, ——, Y. Huang, and M. Zhang, 2014: Observed linkages between the northern annular  
700 mode/North Atlantic Oscillation, cloud incidence, and cloud radiative forcing.  
701 *Geophysical Research Letters*, **41**, 1681–1688, <https://doi.org/10.1002/2013GL059113>.

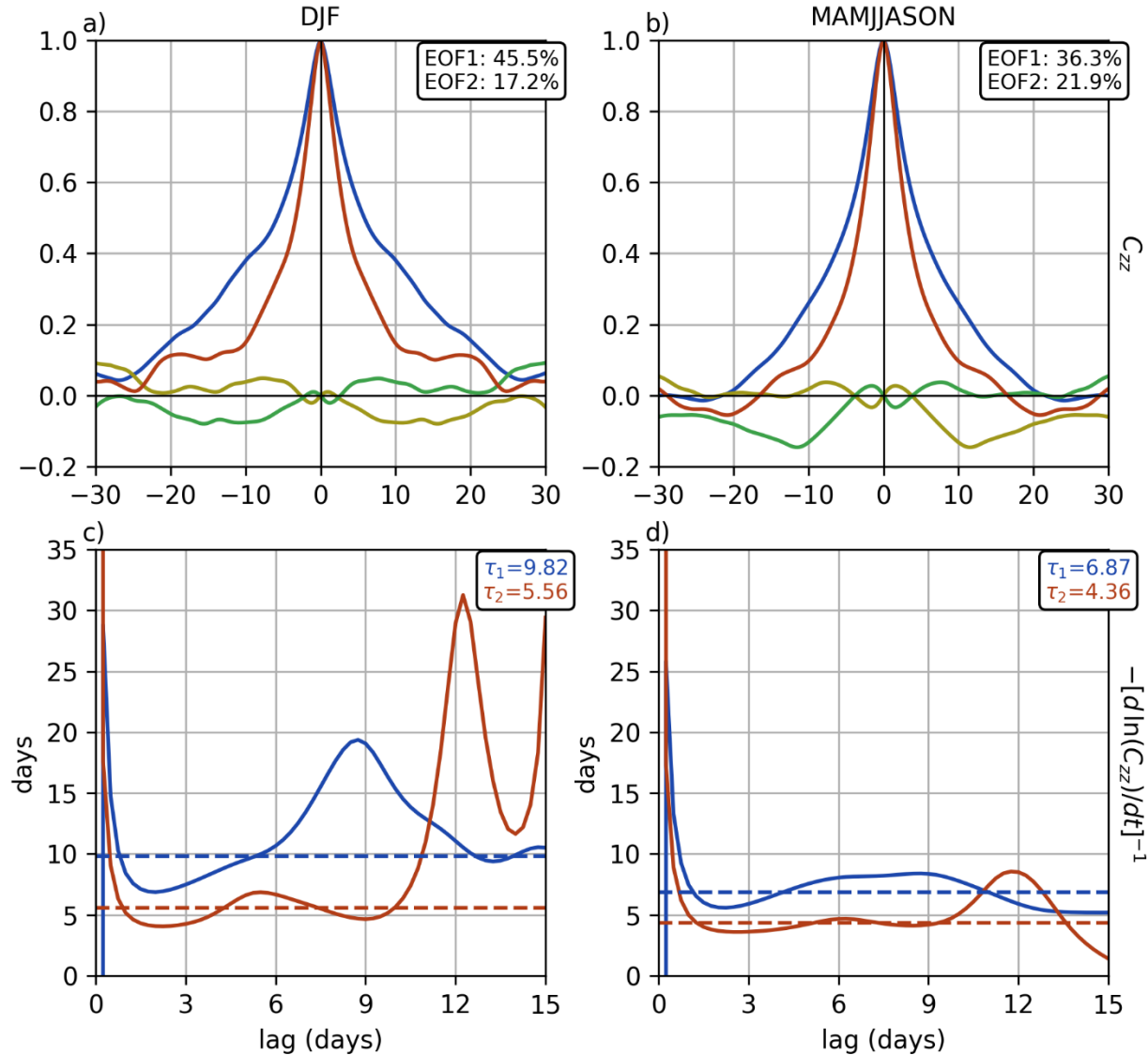
- 702 Liu, S., P. W. Staten, and B. H. Kahn, 2020: Improved Detection of Interannual Cloud Variability  
703 over the Southern Hemisphere Using Legacy Satellites. *Journal of Climate*, **33**, 8225–  
704 8236, <https://doi.org/10.1175/JCLI-D-19-0758.1>.
- 705 Lorenz, D. J., and D. L. Hartmann, 2001: Eddy–Zonal Flow Feedback in the Southern  
706 Hemisphere. *Journal of the Atmospheric Sciences*, **58**, 3312–3327,  
707 [https://doi.org/10.1175/1520-0469\(2001\)058<3312:EZFFIT>2.0.CO;2](https://doi.org/10.1175/1520-0469(2001)058<3312:EZFFIT>2.0.CO;2).
- 708 Lubis, S. W., and P. Hassanzadeh, 2020: An Eddy–Zonal Flow Feedback Model for Propagating  
709 Annular Modes. *Journal of the Atmospheric Sciences*, **78**, 249–267,  
710 <https://doi.org/10.1175/JAS-D-20-0214.1>.
- 711 Lutsko, N. J., and M. C. Hell, 2021: Moisture and the Persistence of Annular Modes. *Journal of*  
712 *the Atmospheric Sciences*, **1**, <https://doi.org/10.1175/JAS-D-21-0055.1>.
- 713 Ma, D., P. Hassanzadeh, and Z. Kuang, 2017: Quantifying the Eddy–Jet Feedback Strength of the  
714 Annular Mode in an Idealized GCM and Reanalysis Data. *Journal of the Atmospheric*  
715 *Sciences*, **74**, 393–407, <https://doi.org/10.1175/JAS-D-16-0157.1>.
- 716 Nakamura, N., and A. Solomon, 2010: Finite-Amplitude Wave Activity and Mean Flow  
717 Adjustments in the Atmospheric General Circulation. Part I: Quasigeostrophic Theory  
718 and Analysis. *Journal of the Atmospheric Sciences*, **67**, 3967–3983,  
719 <https://doi.org/10.1175/2010jas3503.1>.
- 720 ——, and D. Zhu, 2010: Finite-Amplitude Wave Activity and Diffusive Flux of Potential Vorticity  
721 in Eddy–Mean Flow Interaction. *Journal of the Atmospheric Sciences*, **67**, 2701–2716,  
722 <https://doi.org/10.1175/2010jas3432.1>.

- 723 ——, and C. S. Y. Huang, 2017: Local Wave Activity and the Onset of Blocking along a Potential  
724 Vorticity Front. *Journal of the Atmospheric Sciences*, **74**, 2341–2362,  
725 <https://doi.org/10.1175/jas-d-17-0029.1>.
- 726 Nie, Y., Y. Zhang, G. Chen, X.-Q. Yang, and D. A. Burrows, 2014: Quantifying barotropic and  
727 baroclinic eddy feedbacks in the persistence of the Southern Annular Mode. *Geophysical  
728 Research Letters*, **41**, 8636–8644, <https://doi.org/10.1002/2014GL062210>.
- 729 Palipane, E., J. Lu, P. Staten, G. Chen, and E. K. Schneider, 2017: Investigating the zonal wind  
730 response to SST warming using transient ensemble AGCM experiments. *Climate  
731 Dynamics*, **48**, 523–540, <https://doi.org/10.1007/s00382-016-3092-9>.
- 732 Papavasileiou, G., A. Voigt, and P. Knippertz, 2020: The role of observed cloud-radiative  
733 anomalies for the dynamics of the North Atlantic Oscillation on synoptic time-scales.  
734 *Quarterly Journal of the Royal Meteorological Society*, **146**, 1822–1841,  
735 <https://doi.org/10.1002/qj.3768>.
- 736 Riehl, H., T. C. Yeh, and N. E. L. Seur, 1950: A Study of Variations of the General Circulation.  
737 *Journal of the Atmospheric Sciences*, **7**, 181–194, [https://doi.org/10.1175/1520-  
0469\(1950\)007<0181:ASOVOT>2.0.CO;2](https://doi.org/10.1175/1520-<br/>738 0469(1950)007<0181:ASOVOT>2.0.CO;2).
- 739 Ring, M. J., and R. A. Plumb, 2008: The Response of a Simplified GCM to Axisymmetric Forcings:  
740 Applicability of the Fluctuation–Dissipation Theorem. *Journal of the Atmospheric  
741 Sciences*, **65**, 3880–3898, <https://doi.org/10.1175/2008JAS2773.1>.
- 742 Robinson, W. A., 2000: A Baroclinic Mechanism for the Eddy Feedback on the Zonal Index.  
743 *Journal of the Atmospheric Sciences*, **57**, 415–422, [https://doi.org/10.1175/1520-  
0469\(2000\)057<0415:ABMFTE>2.0.CO;2](https://doi.org/10.1175/1520-<br/>744 0469(2000)057<0415:ABMFTE>2.0.CO;2).

- 745 Saggioro, E., and T. G. Shepherd, 2019: Quantifying the Timescale and Strength of Southern  
746 Hemisphere Intraseasonal Stratosphere-troposphere Coupling. *Geophysical Research*  
747 *Letters*, **46**, 13479–13487, <https://doi.org/10.1029/2019GL084763>.
- 748 Sheshadri, A., and R. A. Plumb, 2017: Propagating Annular Modes: Empirical Orthogonal  
749 Functions, Principal Oscillation Patterns, and Time Scales. *Journal of the Atmospheric*  
750 *Sciences*, **74**, 1345–1361, <https://doi.org/10.1175/JAS-D-16-0291.1>.
- 751 Simpson, I. R., and L. M. Polvani, 2016: Revisiting the relationship between jet position, forced  
752 response, and annular mode variability in the southern midlatitudes. *Geophysical*  
753 *Research Letters*, **43**, 2896–2903, <https://doi.org/10.1002/2016GL067989>.
- 754 ——, T. G. Shepherd, P. Hitchcock, and J. F. Scinocca, 2013: Southern Annular Mode Dynamics  
755 in Observations and Models. Part II: Eddy Feedbacks. *Journal of Climate*, **26**, 5220–5241,  
756 <https://doi.org/10.1175/JCLI-D-12-00495.1>.
- 757 Smith, S., P. W. Staten, and J. Lu, 2021: How Moist and Dry Intrusions Control the Local  
758 Hydrologic Cycle in Present and Future Climates. *Journal of Climate*, **34**, 4343–4359,  
759 <https://doi.org/10.1175/JCLI-D-20-0780.1>.
- 760 Son, S.-W., and S. Lee, 2006: Preferred Modes of Variability and Their Relationship with Climate  
761 Change. *Journal of Climate*, **19**, 2063–2075, <https://doi.org/10.1175/JCLI3705.1>.
- 762 Sparrow, S., M. Blackburn, and J. D. Haigh, 2009: Annular Variability and Eddy–Zonal Flow  
763 Interactions in a Simplified Atmospheric GCM. Part I: Characterization of High- and Low-  
764 Frequency Behavior. *Journal of the Atmospheric Sciences*, **66**, 3075–3094,  
765 <https://doi.org/10.1175/2009JAS2953.1>.

- 766 Thompson, D. W. J., and J. M. Wallace, 2000: Annular Modes in the Extratropical Circulation.
- 767           Part I: Month-to-Month Variability. *Journal of Climate*, **13**, 1000–1016,
- 768           [https://doi.org/10.1175/1520-0442\(2000\)013<1000:AMITEC>2.0.CO;2](https://doi.org/10.1175/1520-0442(2000)013<1000:AMITEC>2.0.CO;2).
- 769 ——, ——, and G. C. Hegerl, 2000: Annular Modes in the Extratropical Circulation. Part II:
- 770           Trends. *Journal of Climate*, **13**, 1018–1036, [https://doi.org/10.1175/1520-0442\(2000\)013<1018:AMITEC>2.0.CO;2](https://doi.org/10.1175/1520-0442(2000)013<1018:AMITEC>2.0.CO;2).
- 772 Wang, L., and N. Nakamura, 2015: Covariation of finite-amplitude wave activity and the zonal
- 773           mean flow in the midlatitude troposphere: 1. Theory and application to the Southern
- 774           Hemisphere summer. *Geophysical Research Letters*, **42**, 8192–8200,
- 775           <https://doi.org/10.1002/2015gl065830>.
- 776 Woollings, T., L. Papritz, C. Mbengue, and T. Spengler, 2016: Diabatic heating and jet stream
- 777           shifts: A case study of the 2010 negative North Atlantic Oscillation winter. *Geophysical*
- 778           *Research Letters*, **43**, 9994–10,002, <https://doi.org/10.1002/2016GL070146>.
- 779 Xia, X., and E. K. M. Chang, 2014: Diabatic Damping of Zonal Index Variations. *Journal of the*
- 780           *Atmospheric Sciences*, **71**, 3090–3105, <https://doi.org/10.1175/JAS-D-13-0292.1>.
- 781 Zurita-Gotor, P., J. Blanco-Fuentes, and E. P. Gerber, 2014: The Impact of Baroclinic Eddy
- 782           Feedback on the Persistence of Jet Variability in the Two-Layer Model. *Journal of the*
- 783           *Atmospheric Sciences*, **71**, 410–429, <https://doi.org/10.1175/JAS-D-13-0102.1>.
- 784

785 **Figures**



786

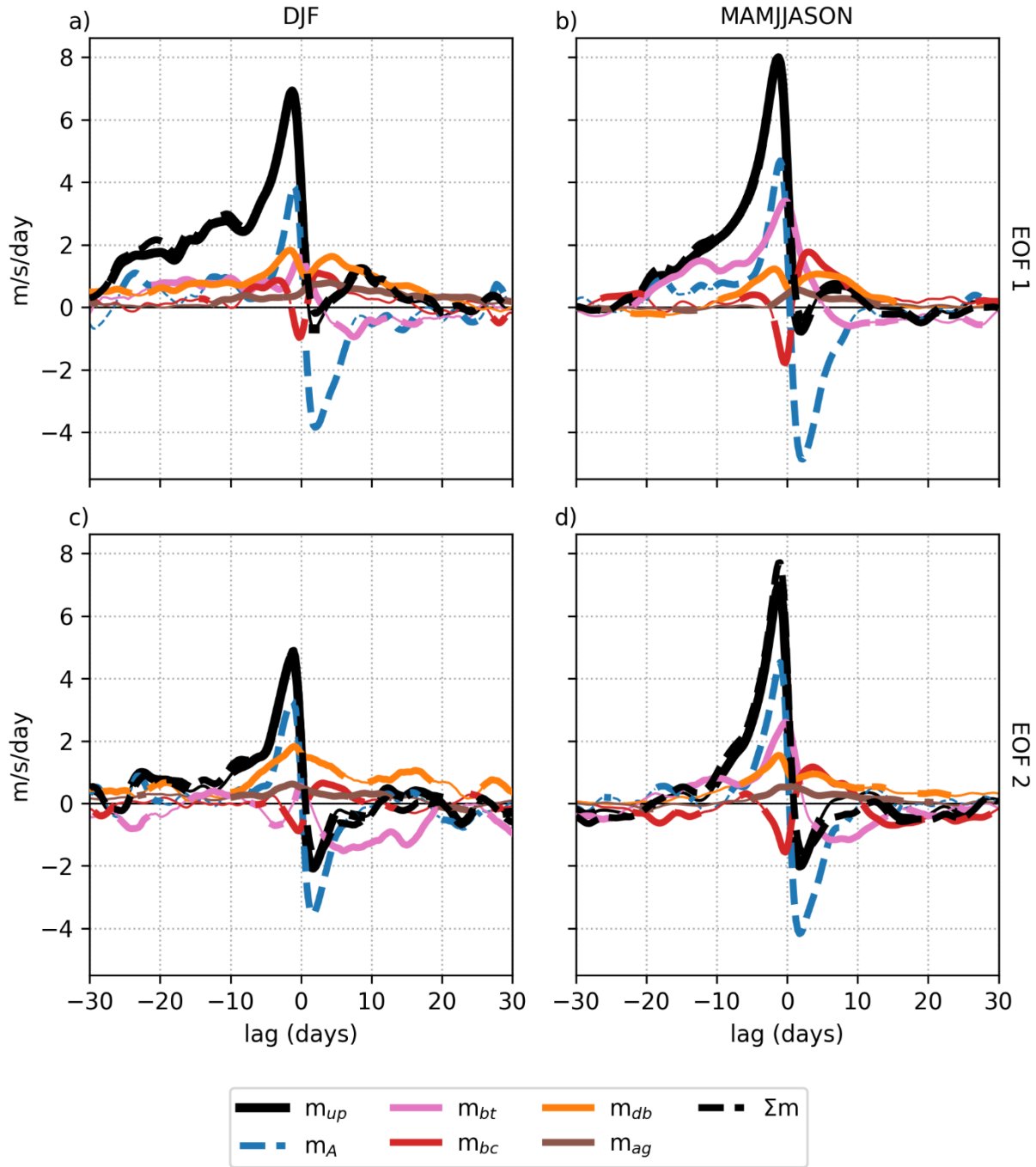
EOF

—	1->1	—	1->2	—	2->1	—	2->2
---	------	---	------	---	------	---	------

787 Figure 1: Lead-lag regressions of EOF 1 and 2 timeseries of zonal-wind onto themselves and  
 788 each other, for a) December-January (DJF) and b) March-November (MAMJJASON) from 2005-  
 789 2019 in MERRA2. Also listed is the variance explained by each mode (normalized eigenvalue).

790 The bottom row shows the smoothed, implied decorrelation timescale (assuming exponential  
791 decay) for the EOF 1 and 2 autocorrelations as a function of lag (solid lines) for c) DJF and d)  
792 MAMJJASON, as well as the mean decorrelation timescale produced by fitting an exponential  
793 decay function to the autocorrelations in panels a) and b).

794



795

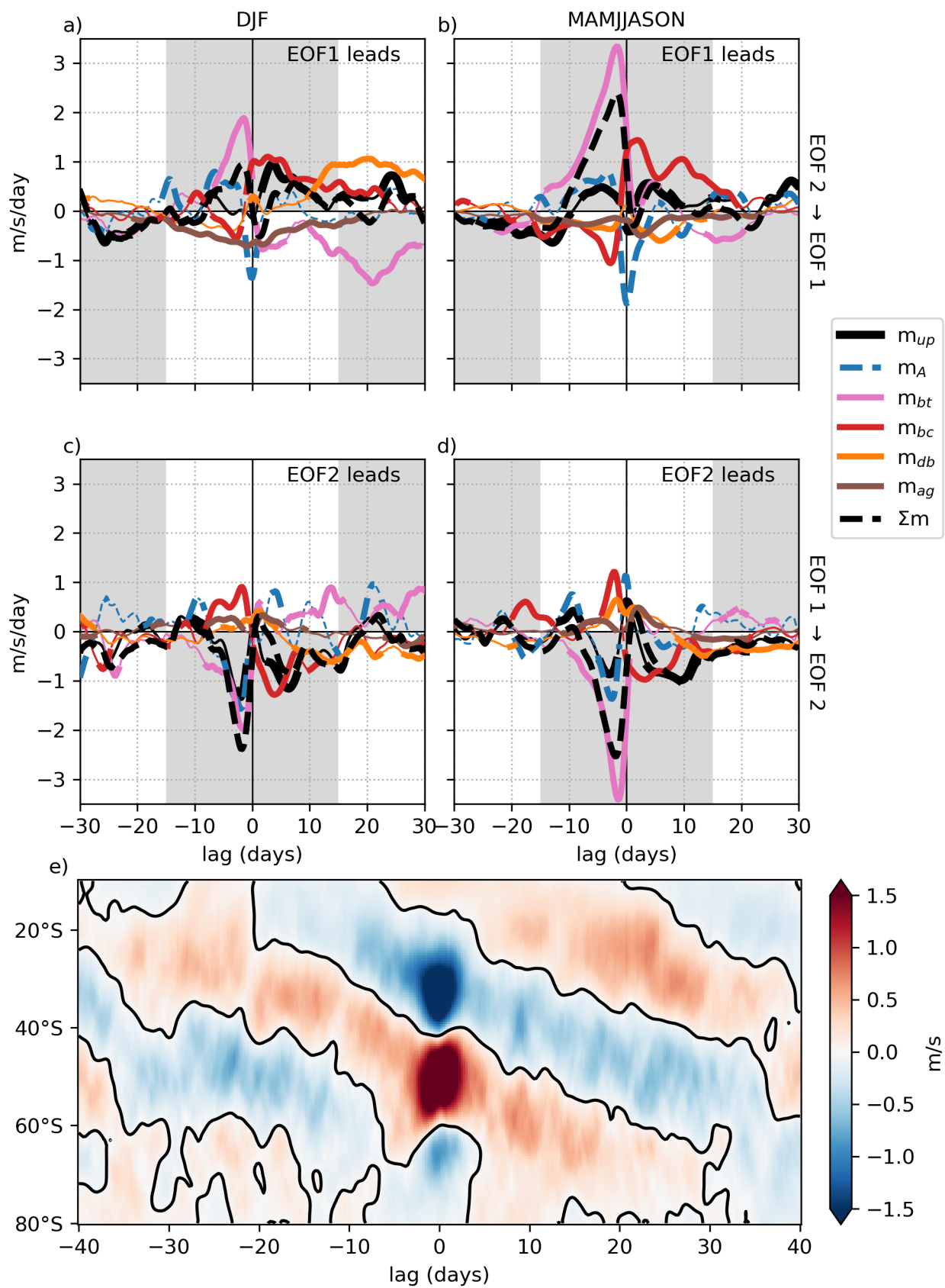
796 Figure 2: The upper-level (500-100hPa) vertically-integrated eddy momentum flux convergence

797 (EMFC) budget as a function of lag in 6-hourly MERRA2 data for 2005-2019. The EMFC budget is

798 separated into DJF (a) and MAMJJASON (b) in EOF1 and DJF (c) and MAMJJASON (d) in EOF2.

799  $m_{up}$  is the upper-level eddy momentum flux convergence projected onto the SAM,  $m_A$  is the

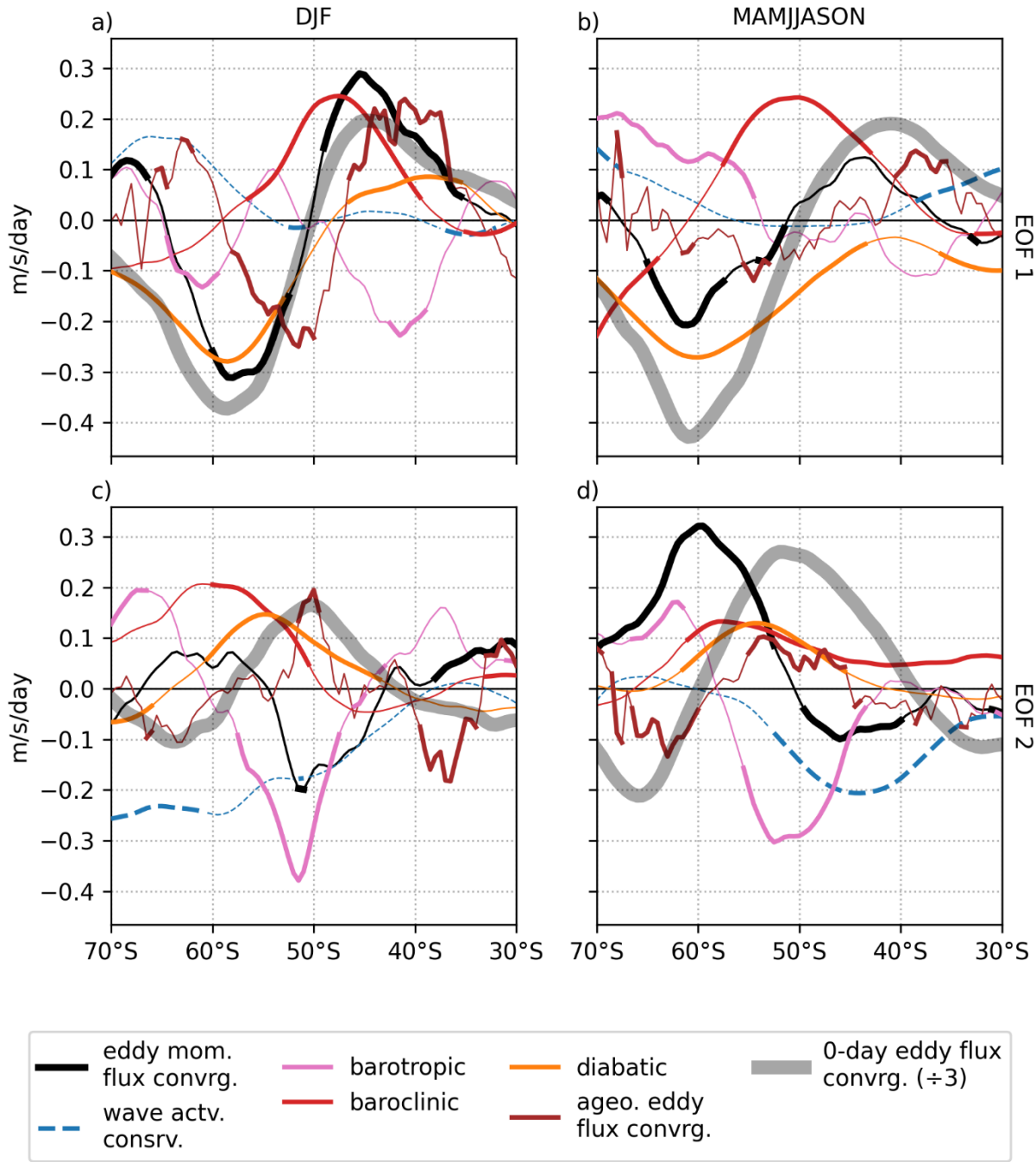
800 component of  $m_{up}$  driven by the conservation of wave activity (angular pseudo-momentum),  
801  $m_{bt}$  is the “barotropic” component of  $m_{up}$  driven by irreversible potential vorticity mixing,  $m_{bc}$   
802 is the “baroclinic” component of  $m_{up}$  from the eddy heat flux convergence [the vertical  
803 component of the Eliassen-Palm flux divergence],  $m_{db}$  is the “diabatic” component of  $m_{up}$   
804 driven by latent and radiative heating,  $m_{ag}$  are the ageostrophic contributions to  $m_{up}$ , and  
805  $\sum m = m_A + m_{bt} + m_{bc} + m_{db} + m_{ag}$  is the reconstruction of  $m_{up}$ , which is frequently on top  
806 of  $m_{up}$ . Lines appear thin where the bootstrapped 90% confidence interval contains zero.  
807



809 Figure 3: Panels (a-d): As in Figure 2, but for the EMFC of EOF2 regressed against EOF1 (top) and  
810 the EMFC of EOF1 regressed onto EOF2 (bottom) for DJF (left) and MAMJJASON (right). Grey  
811 shaded regions denote signals of poleward propagation of anomalies (positive EOF1 followed  
812 by positive EOF2, followed by negative EOF1, and finally negative EOF2), while white regions  
813 denote tendencies toward equatorward propagation. Panel (e) shows a composite of zonal-  
814 mean zonal angular momentum anomalies during 81 propagation events identified using the  
815 method outlined in Section 3.1 from MERRA2 during 2005-2019.

816

lag day 10



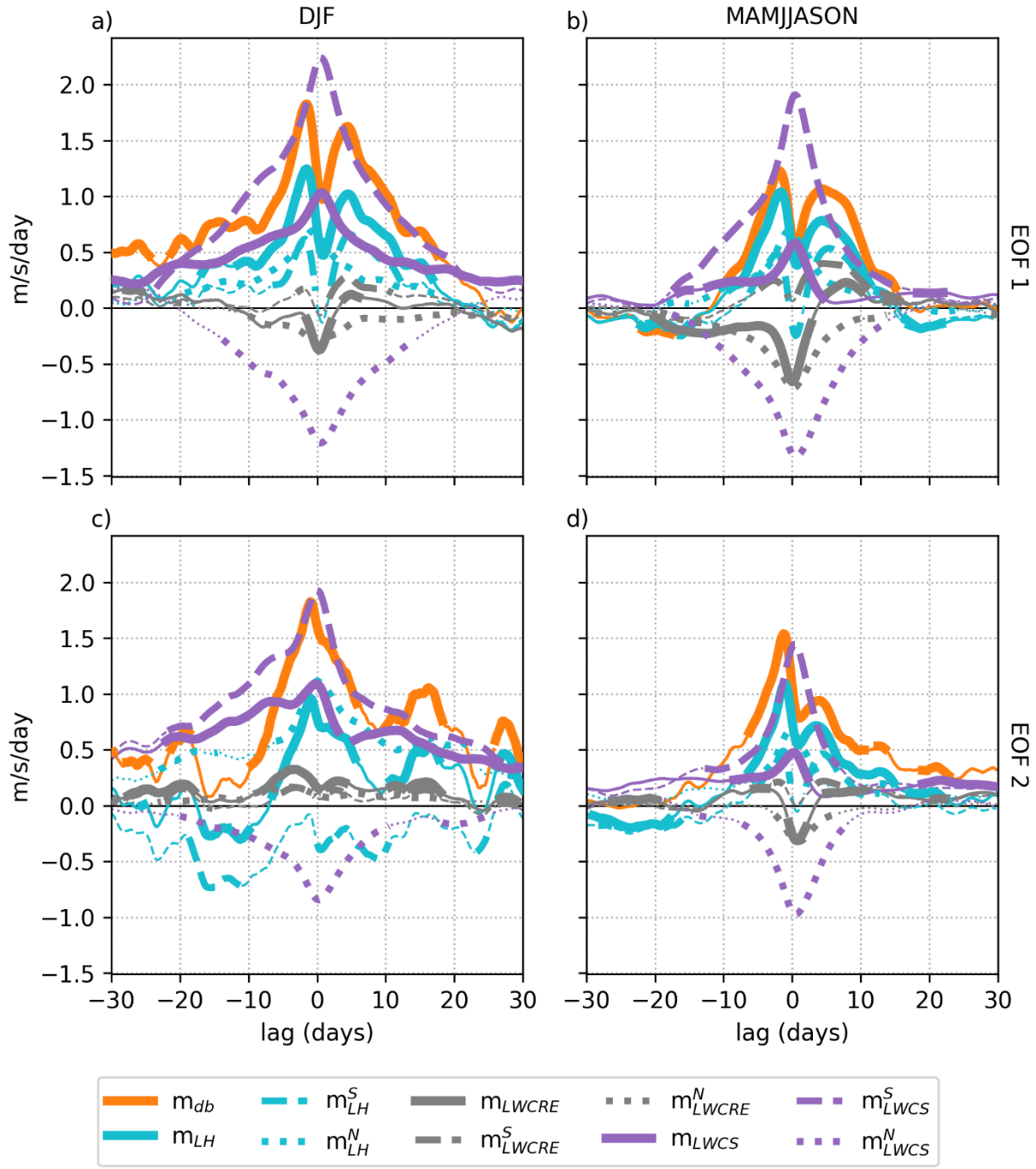
817

818 Figure 4: The latitudinally-varying components of the EMFC budget depicted in Figure 2,  
 819 regressed onto the EOF1 for (a) DJF and (b) MAMJJASON and onto EOF2 for (c) DJF and (d)  
 820 MAMJJASON at a 10-day lag. For reference, the thick grey line shows the peak eddy momentum

821 flux convergence at day zero, reduced in magnitude by one-third. As before, lines appear thin

822 where the bootstrapped 90% confidence interval contains zero.

823



824

825 Figure 5: As in Figure 2, but the upper-level EMFC contributed by different diabatic processes.

826  $m_{db}$  is the same diabatic component of  $m_{up}$  as Figure 2, calculated as the sum of the following

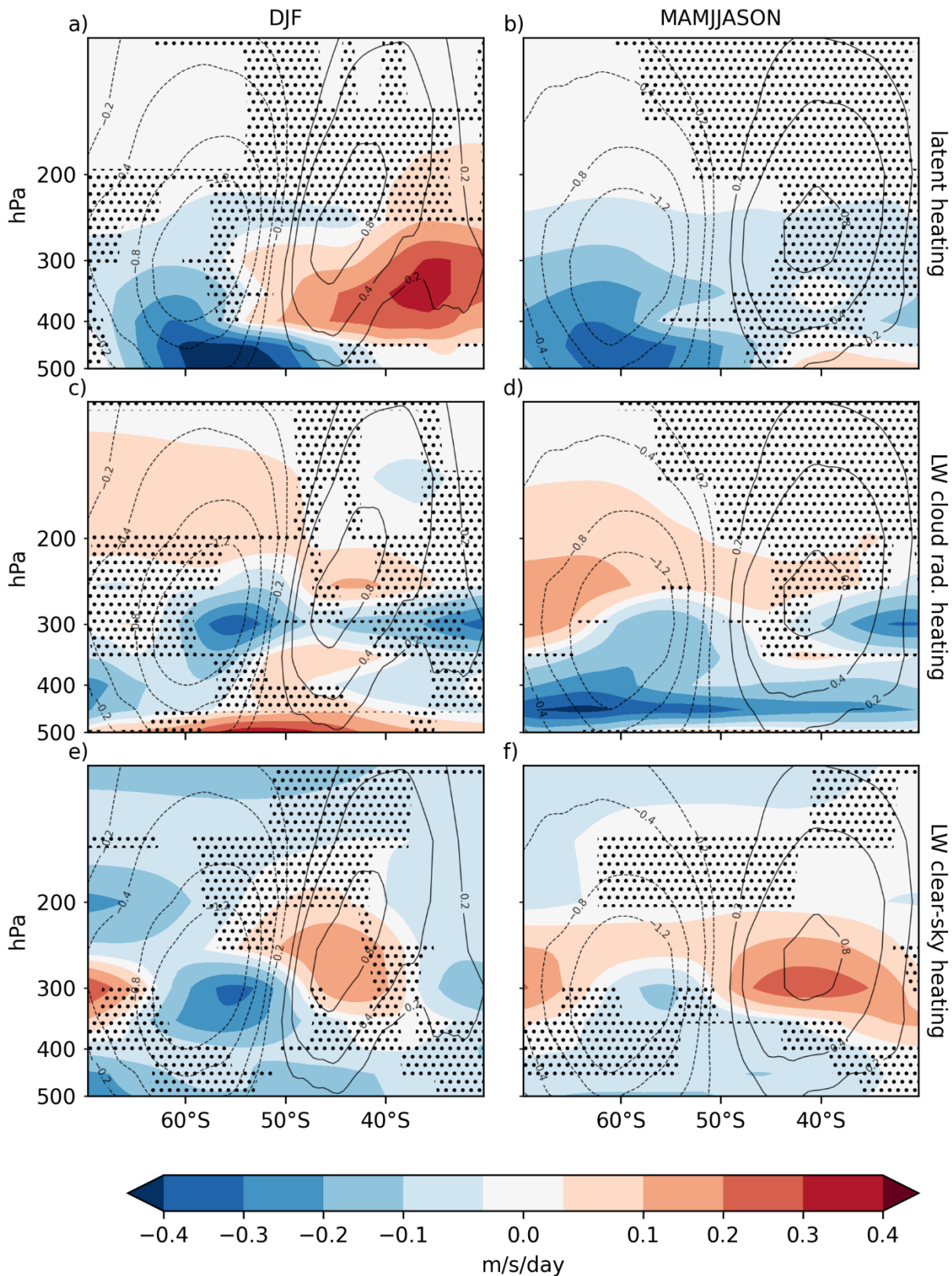
827 terms.  $m_{LH}$  is the component of  $m_{up}$  driven by latent heat release,  $m_{LWCRE}$  is the component

828 of  $m_{up}$  driven by longwave (LW) cloud radiative heating (all-sky minus clear-sky), and  $m_{LWCS}$  is

829 the component of  $m_{up}$  driven by LW clear-sky radiative heating. Shortwave cloud and clear-sky  
830 cooling are included in  $m_{db}$ , but they are left for Supplemental Figure 2 as they are negligible.  
831 Also shown separately are contributions from anticyclonic (southward) wave breaking  
832 (superscript S) and cyclonic (northward) wave breaking (superscript N).

833

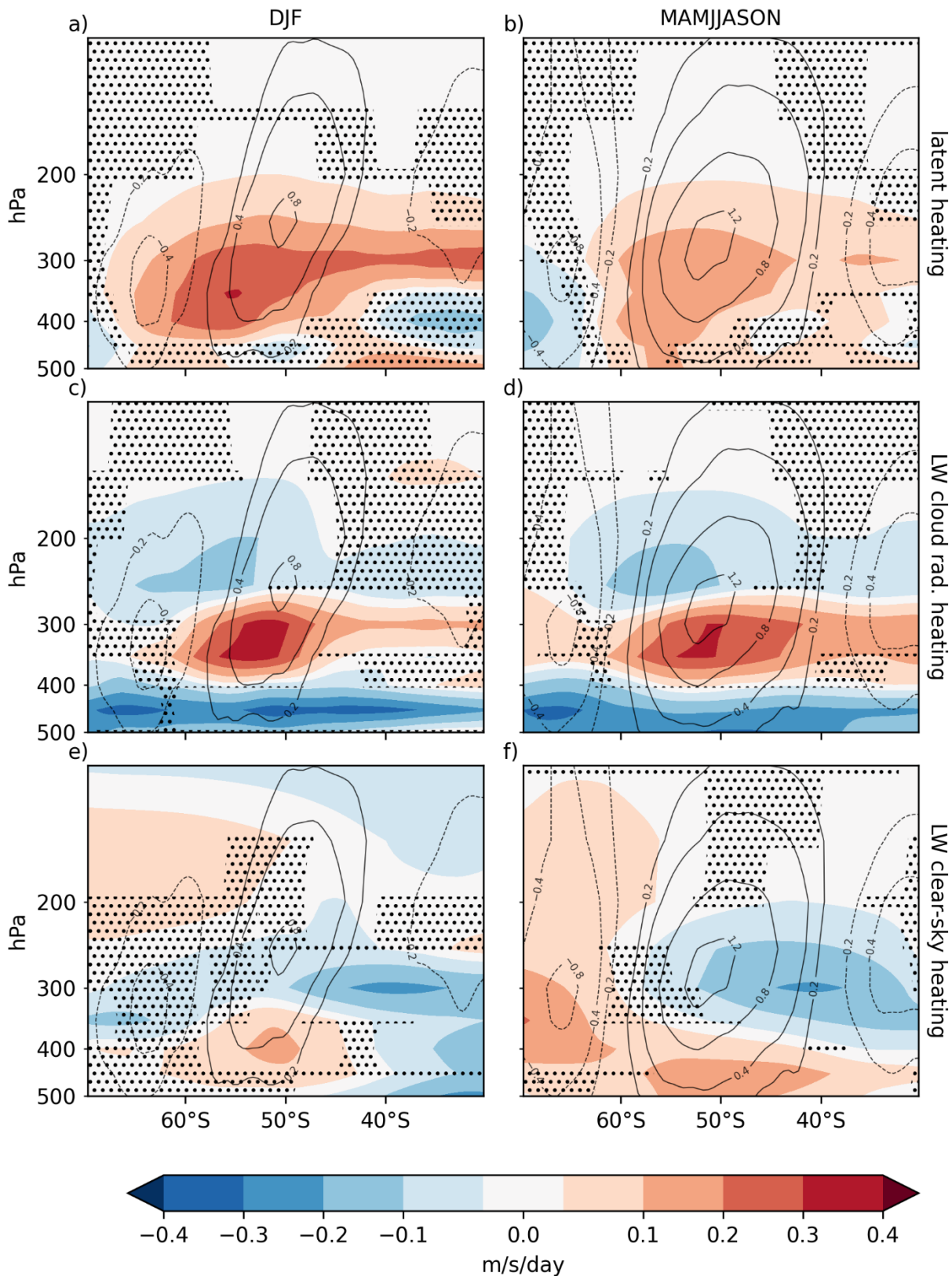
### EOF 1, 10-day lag



835 Figure 6: The diabatic components of the EMFC budget depicted in Figure 5, regressed onto the  
836 EOF1 index at a 10-day lag (shading). EMFC contributions are shown from (a,b) latent heating  
837 ( $m_{LH}$ ), (c,d) cloud longwave heating ( $m_{LWCRE}$ ), and clear-sky longwave heating ( $m_{LWCS}$ ) for DJF  
838 and MAMJJASON, respectively. Contours are the eddy momentum flux convergence at day zero  
839 (in m/s/day) for reference. Stippling represents regions where bootstrapped 90% confidence  
840 intervals contain zero.

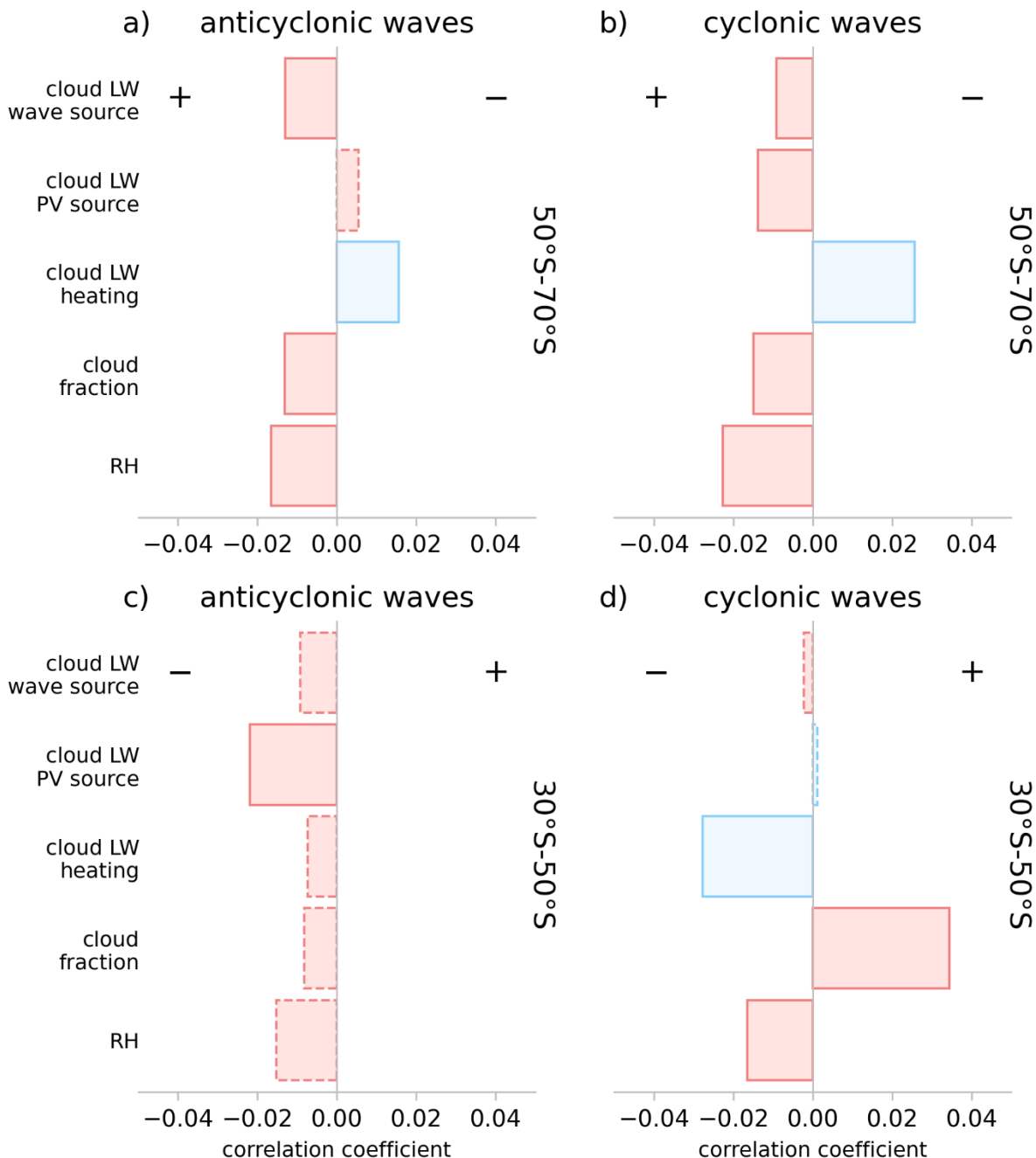
841

EOF 2, 10-day lag



843     Figure 7: As in Figure 6, but regressed against the EOF2 index.

844

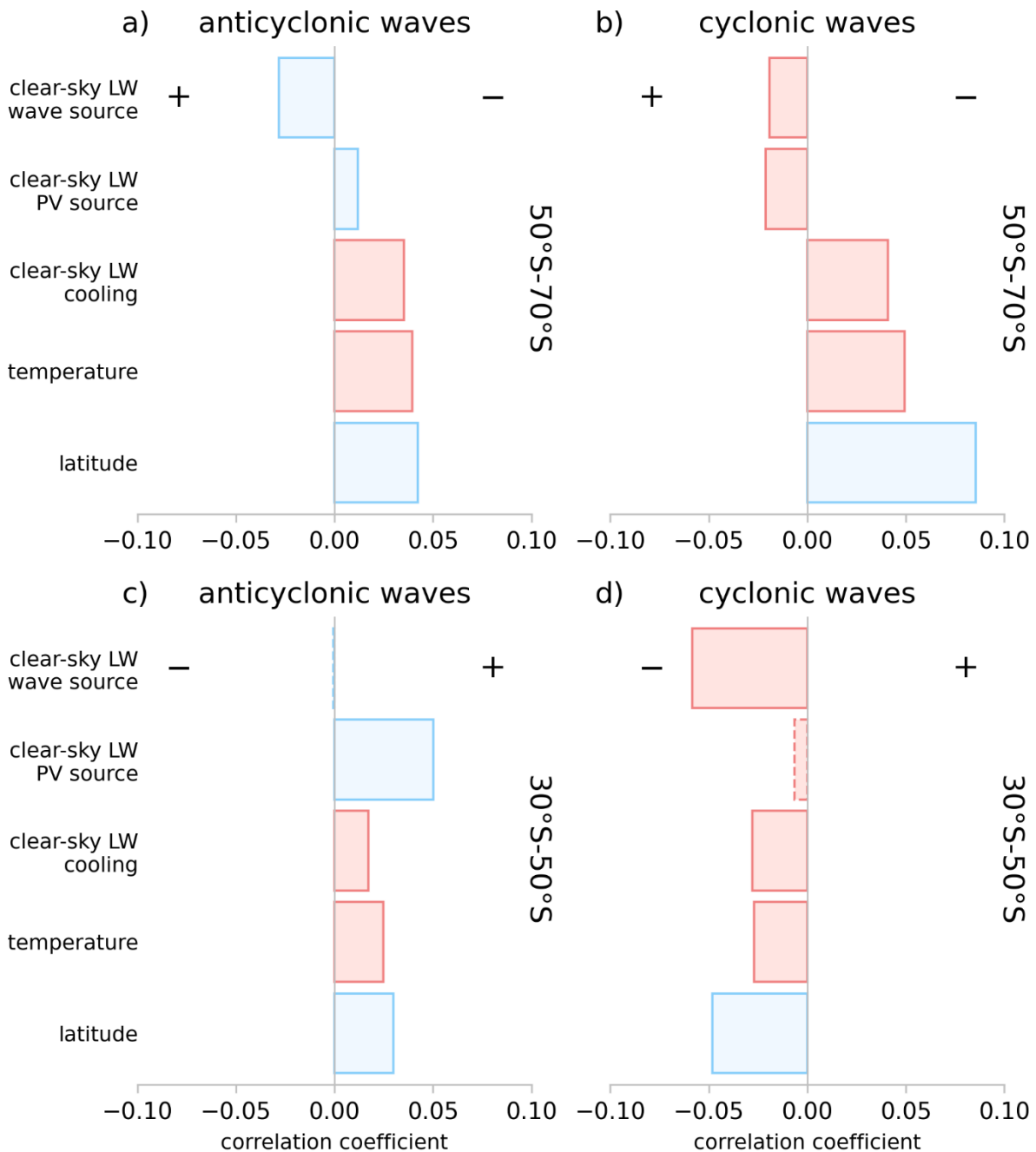


845

846 Figure 8: Correlation coefficients of EOF1 with the 10-day-lagged, 500-100hPa-averaged, year-  
 847 round relative humidity, cloud fraction, longwave cloud heating, the longwave cloud heating PV  
 848 source, and the longwave cloud contribution to the EMFC for a) anticyclonic wave regions,  
 849 between 50-70 degrees south, b) cyclonic wave regions, between 50-70 degrees south, c)

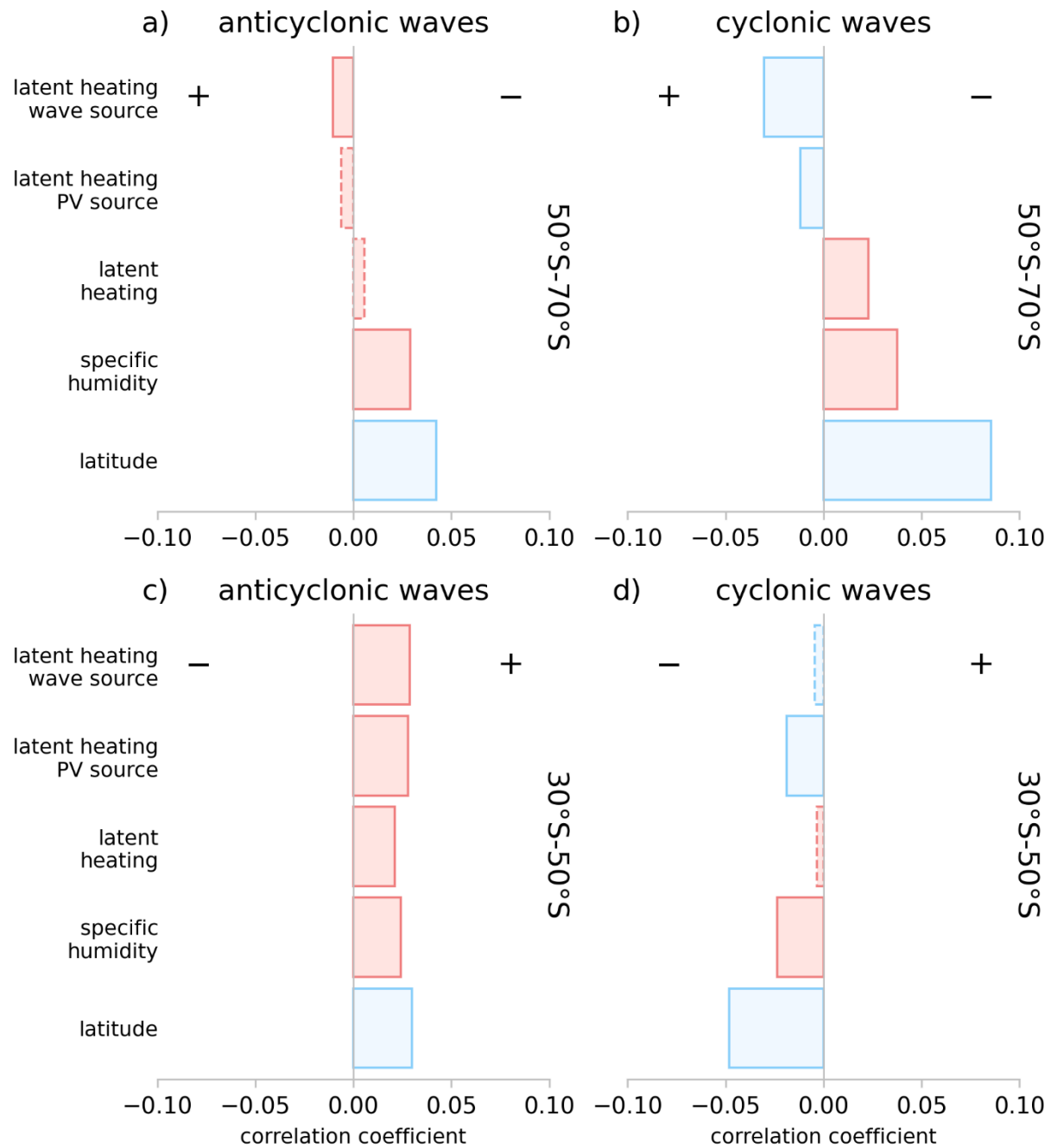
850 anticyclonic wave regions, between 30-50 degrees south, and d) cyclonic wave regions,  
851 between 30-50 degrees south. Blue shading indicates that the mean value of the field for each  
852 composite region is negative; red shading indicates the mean value is positive. Signs are chosen  
853 for the PV source and wave activity source fields to match the sign of the PV anomaly, i.e. a  
854 positively correlated PV source for anticyclonic waves corresponds to anticyclonic  
855 strengthening, whereas a positively correlated source for cyclonic waves corresponds to  
856 cyclonic strengthening. Plus/minus signs by the wave activity source correlations indicate  
857 whether the changes are same-signed (+) or opposite-signed (-) as the SAM momentum  
858 anomalies (i.e., either a positive or a negative feedback). Dashed outlines are not significant  
859 correlations at the 95% confidence level.

860



861

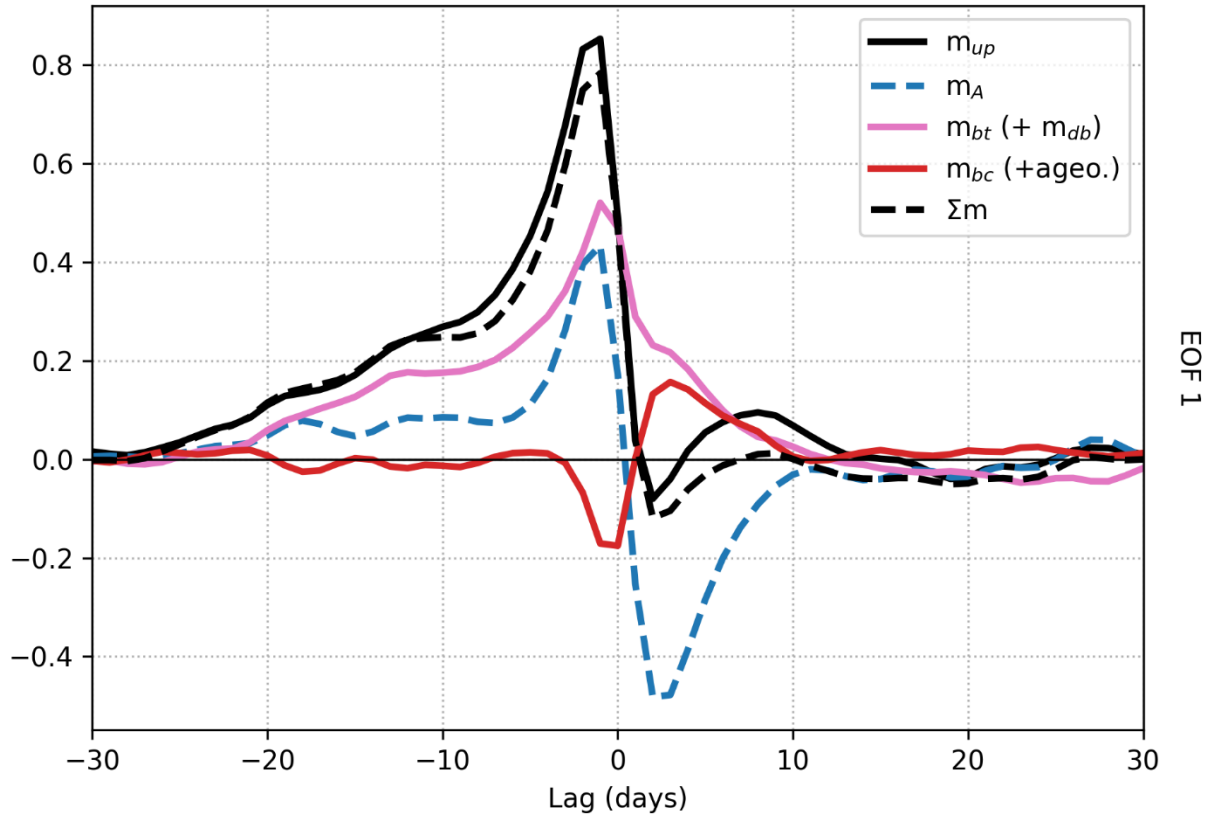
862 Figure 9: As in Figure 8, but for 500-100 hPa centroid latitude, temperature, longwave clear-sky  
 863 cooling (negative heating), longwave clear-sky PV source, and longwave clear-sky EMFC  
 864 contribution. The sign convention for PV sources and wave sources is the same as Figure 8.  
 865



866

867 Figure 10: As in Figure 8, but for 500-100 hPa centroid latitude, specific humidity, latent heating  
 868 tendency, latent heating potential vorticity source, and latent heating contributions to the  
 869 EMFC.

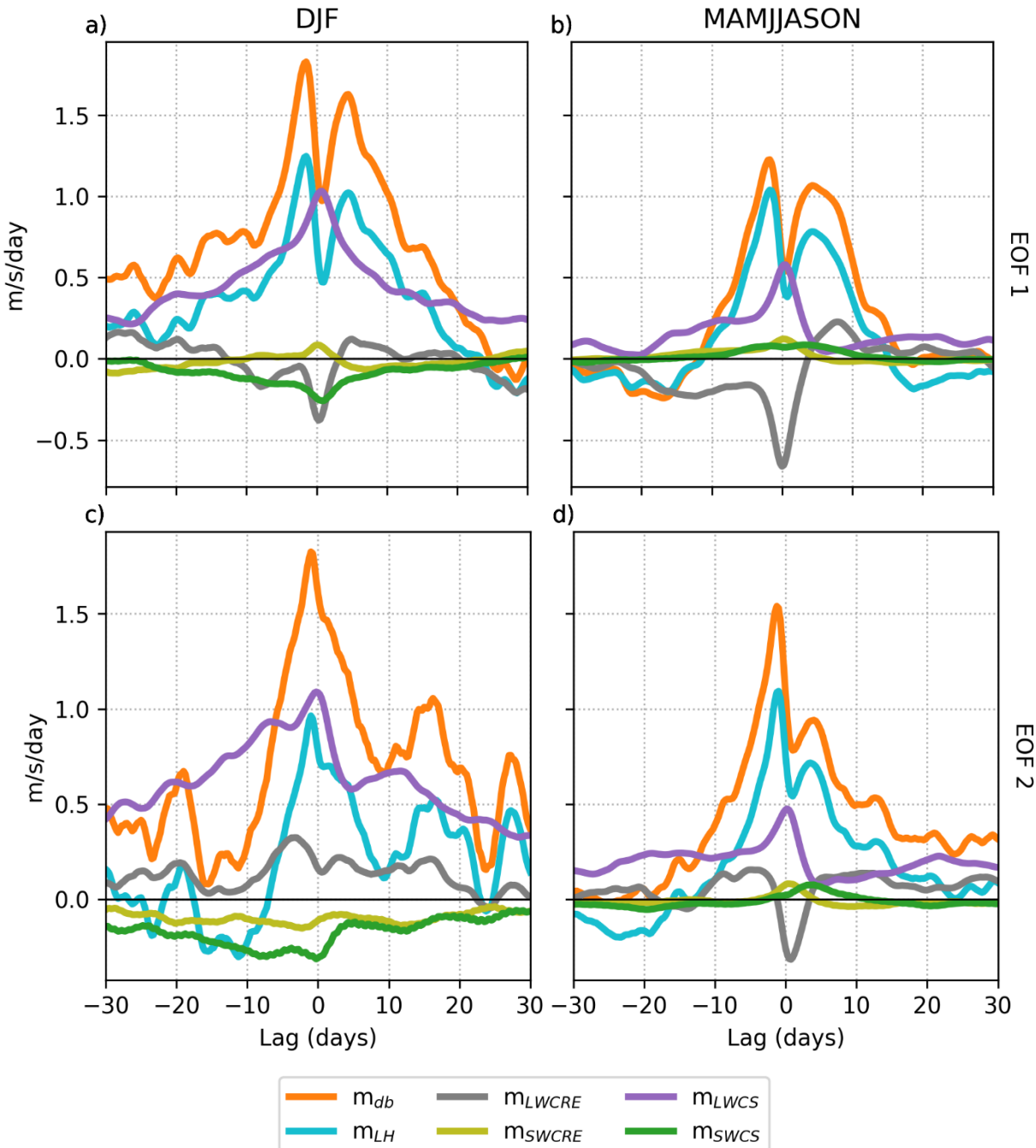
870

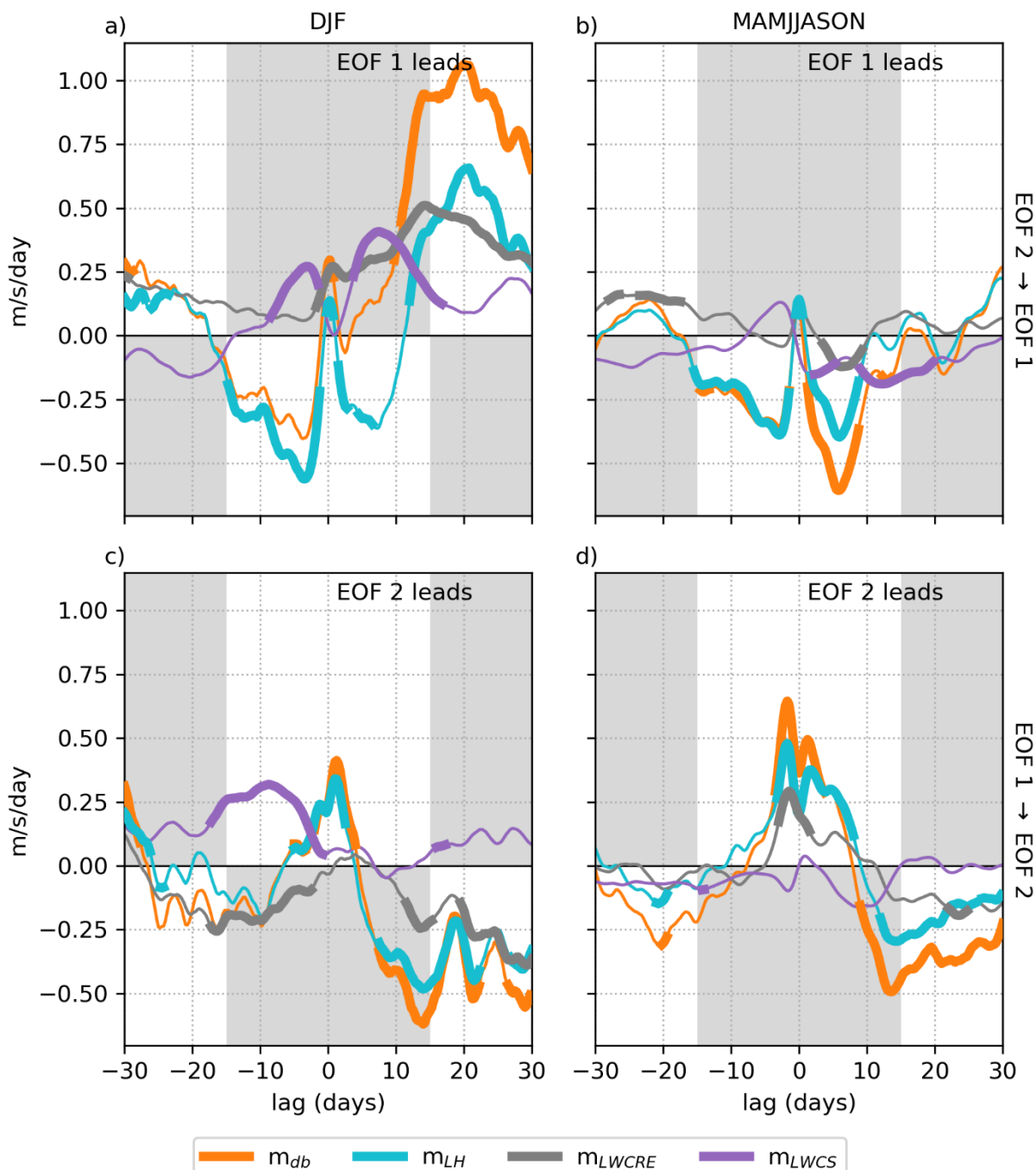
871 **Supplemental Figures**

872  
 873 Figure S1: As in Figure 2, but in the style of Nie et al. (2014; see their Figure 2a)'s budget of the  
 874 eddy momentum flux convergence, produced using the year-round MERRA2 data from 2005-  
 875 2019 used for this study, only for EOF1. To match the magnitudes obtained by Nie et al. (2014),  
 876 we down-sample the 6-hourly data to daily, while also coarsening the latitudinal resolution  
 877 from  $0.5^\circ$  to  $2.5^\circ$  since the magnitude of a linear projection is sensitive to the horizontal  
 878 resolution (see section 4.1). The PC index is taken to vary from -1 to 1 instead of having unit  
 879 variance. Finally, we combine  $m_{db} + m_{bt}$  for  $m_{bt}$  and take the full eddy heat flux rather than  
 880 just the geostrophic for  $m_{bc}$  (see section 2).

881

SAM momentum

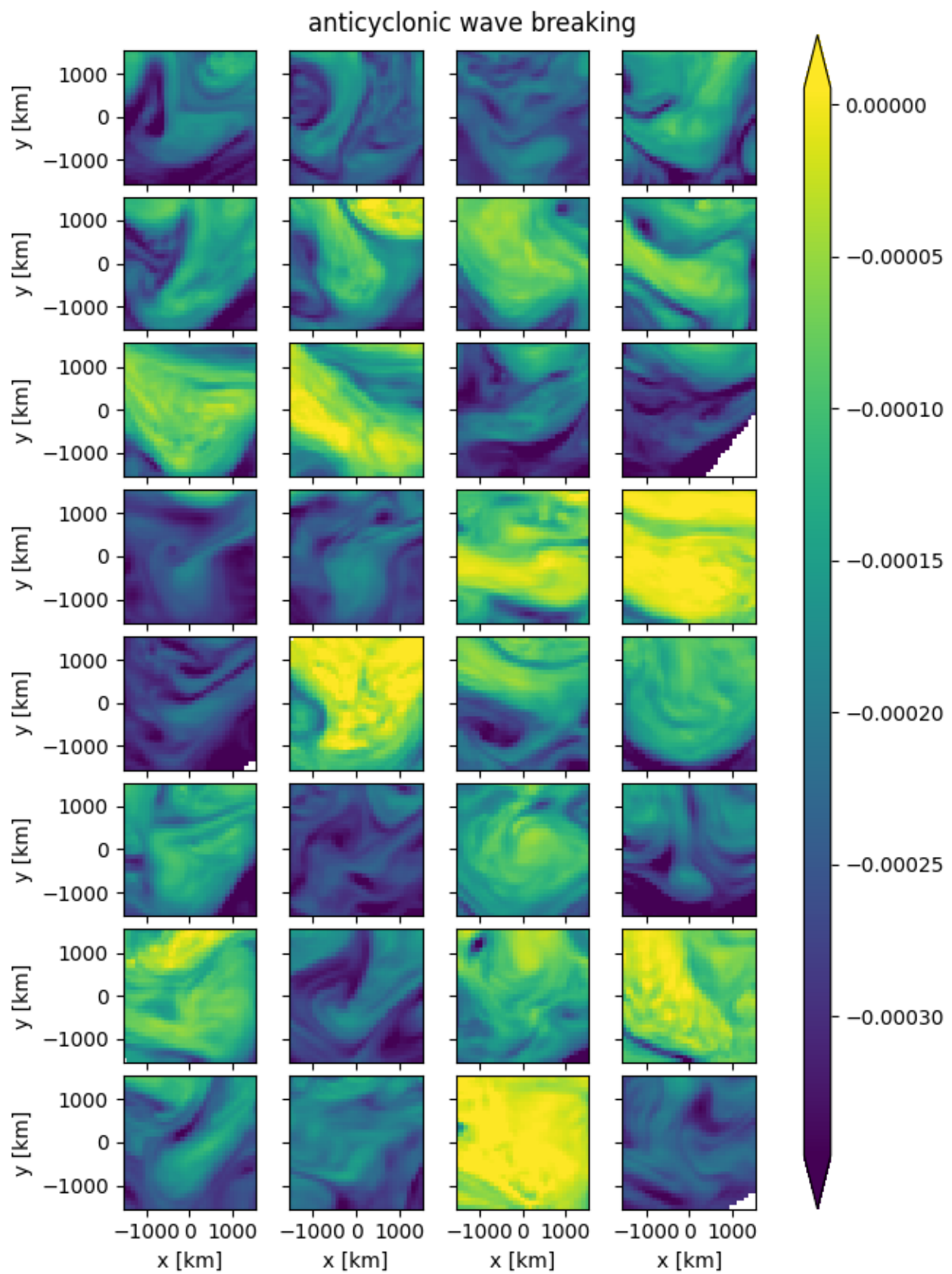




888

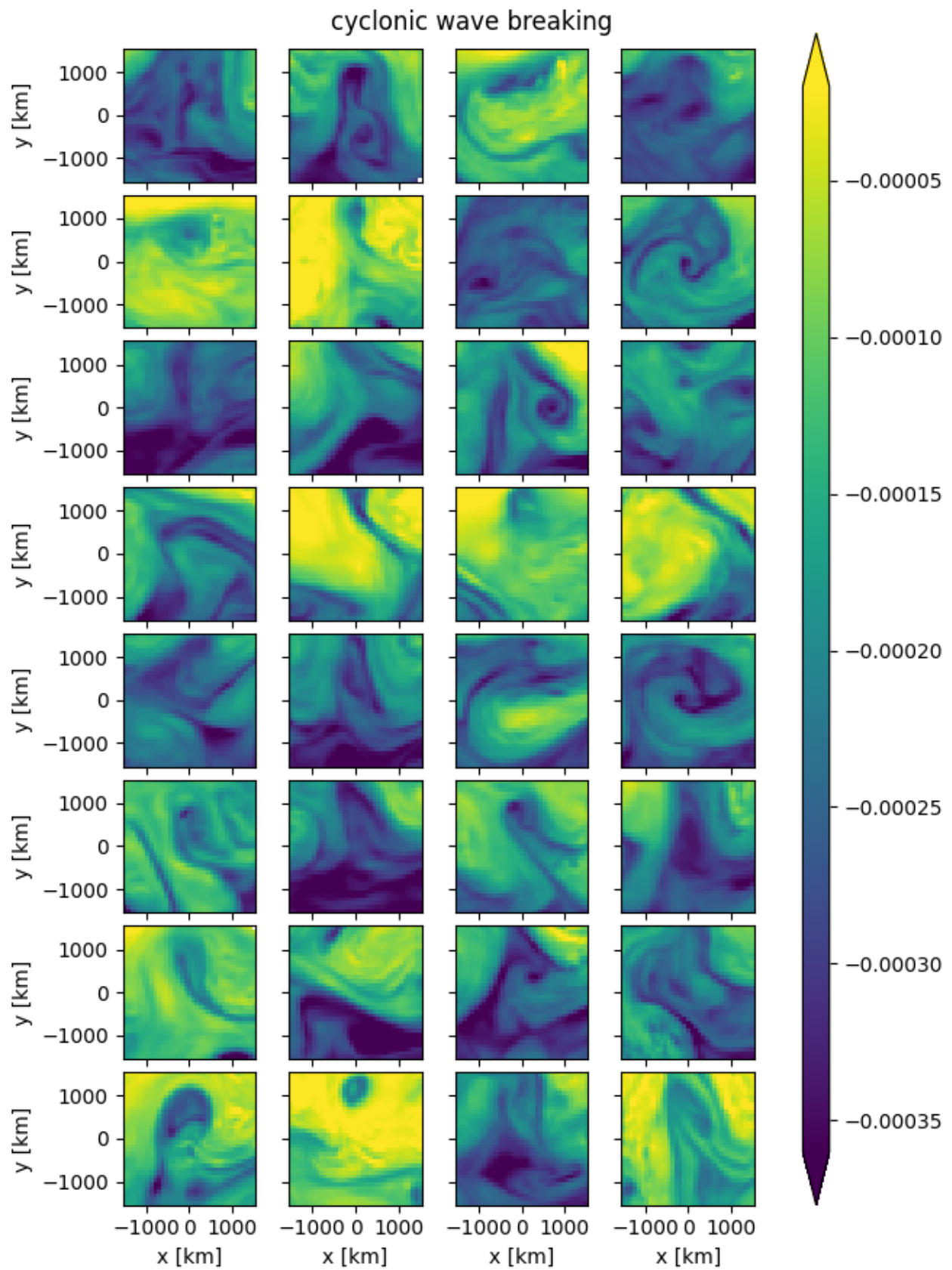
889

Figure S3: As in Figure 3a-d, but for each diabatic process separately (as in Figure 5).



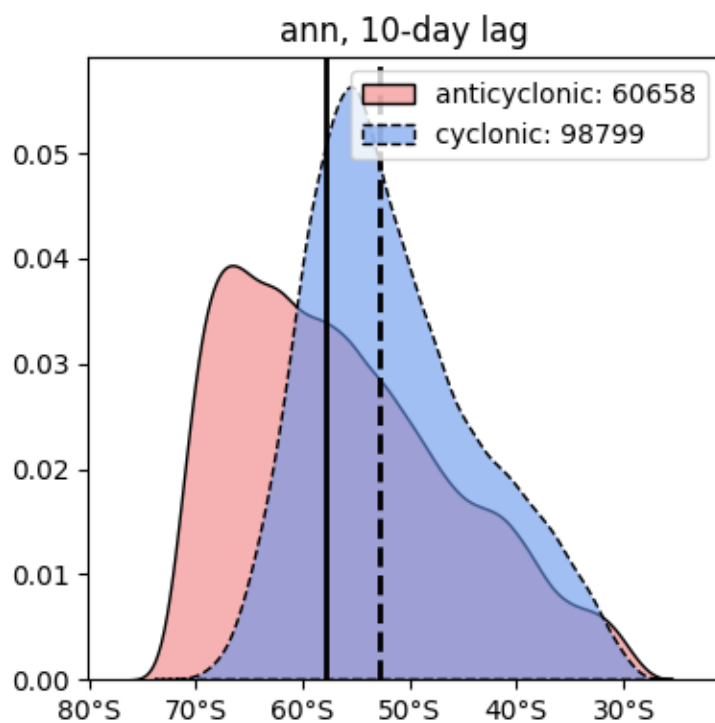
891 Figure S4: A random sample of anticyclonic wave breaking events identified by the wave activity  
892 tracking procedure described in section 3.2 for MERRA2 from 2005-2019. Shading is quasi-  
893 geostrophic potential vorticity taken at the same time and with the same central  
894 latitude/longitude as identified in the wave activity field. The x-coordinate is positive eastward,  
895 and the y-coordinate is positive northward. Missing values result when the data is too close to  
896 the pole to be properly interpolated.

897  
898



900     Figure S5: As in Figure S3, but for cyclonic wave breaking events.

901



902  
 903 Figure S6: Probability distribution functions (PDFs) showing the counts and distribution of  
 904 cyclone and anticyclone central latitudes in MERRA2 (2005-2019) identified using the method  
 905 outlined in section 3.2. Distributions are year-round and for cyclones/anticyclones used in the  
 906 10-day lagged analysis of section 4.3. Black vertical lines represent the medians for the  
 907 anticyclonic (solid) and cyclonic (dashed) waves. Note that latitudes are technically equivalent  
 908 latitudes (c.f. Huang and Nakamura, 2016).  
 909